Chapter

PV PANEL MODELING AND IDENTIFICATION

***Li Hong Idris Lim*[1,*], *Zhen Ye*[2] , *Dazhi Yang*[3]**
***and Han Chong Shaun Tay*[4]**
[1]School of Engineering, University of Glasgow, Glasgow, UK
[2]Renewable Energy Corporation (REC), Singapore
[3]Singapore Institute of Manufacturing Technology, Singapore
[4]Singapore Institute of Technology, Singapore

Abstract

In this chapter, the modelling techniques of PV panels from I-V characteristics are discussed. At the beginning, a necessary review on the various methods are presented, where difficulties in mathematics, drawbacks in accuracy, and challenges in implementation are highlighted. Next, a novel approach based on linear system identification is demonstrated in detail. Other than the prevailing methods of using approximation (analytical methods), iterative searching (classical optimization), or soft computing (artificial intelligence), the proposed method regards the PV diode model as the equivalent output of a dynamic system, so the diode model parameters can be linked to the transfer function coefficients of the same dynamic system. In this way, the problem of solving PV model parameters is equivalently converted to system identification in control theory, which can be perfectly solved by a simple integral-based linear least square method. Graphical meanings of the proposed method are illustrated to help readers understand the underlying principles. As compared to other methods, the proposed one has the following benefits: 1) unique solution; 2) no iterative or global searching; 3) easy to implement (linear least square); 4) accuracy; 5) extendable to multi-diode models. The effectiveness of the proposed method has been verified by indoor and outdoor PV module testing results. In addition, possible applications of the proposed method are discussed like online PV monitoring and diagnostics, non-contact measurement of POA irradiance and cell temperature, fast model identification for satellite PV panels, and etc.

[*]E-mail address: LiHonIdris.Lim@glasgow.ac.uk

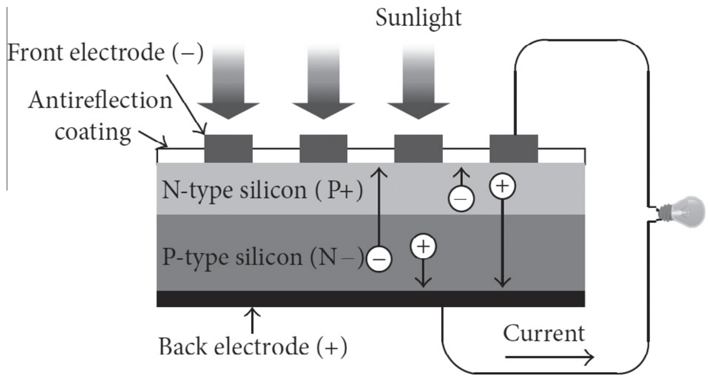

Figure 1. Equivalent circuit of diode models.

1. Introduction

PV panels are made of PV cells assembled in series/parallel and encapsulated in modules. The cell structure can be simplified as a *p-n* junction exposed to light, as depicted in Figure 1, which is a combination of two layers of differently doped semiconductor materials.

1.1. PV Modeling

Without the sunlight, the characteristics of the *p-n* junction is governed by the well-known Shockley diode equation [1]

$$I_D = I_o \left(e^{\frac{V}{a}} - 1 \right), \tag{1}$$

where I_D is the diode current, I_o is the reverse saturation current, $a = nkT_c/q$ is the modified ideality factor [2], n is the ideality factor, k is Boltzmann's constant (1.380653×10^{-23} J/K), T_c is the cell temperature, and q is the electron charge ($1.60217646 \times 10^{-19}$ C). With the presence of sunlight, the *p-n* junction absorbs the photon and generates electron-hole pairs (or carriers) moving across the junction, which is known as the photovoltaic effect. The inclusion of the resulted photocurrent into Shockley equation (1) forms an ideal model of PV cells as

$$I = I_L - I_D = I_L - I_o \left(e^{\frac{V}{a}} - 1 \right), \tag{2}$$

where photocurrent I_L is dependent on the flux of incident irradiation as well as the absorption capacity of the semiconductor materials [3]. However, the ideal model by (2) usually yields unacceptable errors in reality due to the lack of consideration on the current losses from the contact resistance between the silicon and electrodes surfaces, the current flow resistance in the silicon material and the resistance of the electrodes. By incorporating the effects from all these resistances, a more realistic and accurate model [4] is derived as

$$I = I_L - \sum_{i=1}^{m} I_{D_i} - I_{sh} = I_L - \sum_{i=1}^{m} I_{o_i} \left(e^{\frac{V+R_sI}{a_i}} - 1 \right) - \frac{V + R_sI}{R_{sh}}, \tag{3}$$

where R_s and R_{sh} are resistances in series and parallel,respectively. The equivalent circuit for (3) is shown in Figure 2, where diode D_1 accounts for carriers diffusing across the *p*-

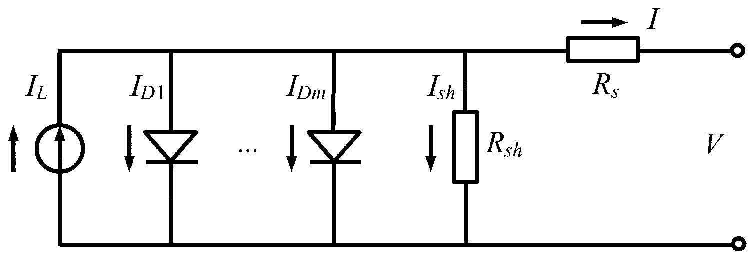

Figure 2. Equivalent circuit of diode models.

n junction and recombining in the bulk or at surfaces, diode D_2 is sometimes attributed to carrier recombination by traps within the depletion region [5], or recombination at an unpassivated cell edge [6]. Theoretically, more diodes ($m > 2$) can be added to the circuit in Figure 2 to better account for distributed and localized effects in solar cells like Auger recombination, but their contributions are negligible as compared to D_1 and D_2 [7].

Note that (3) is applicable not only to PV cells, but also to PV modules. For the latter, $a_i = N_s n_i k T_c / q$, where N_s is the number of cells connected in series. In the lumped-circuit model by (3) or Figure 2, only I and V are known variables from the data sheet or real measurements. The model identification is then to determine the unknown parameters I_L, I_{o_i}, a_i, R_s and R_{sh} from the known data of I and V.

1.2. PV Model Identification

Even in the case of the one diode model ($m = 1$ in (3)), it is not straightforward to determine the model parameters (I_L, I_o, a, R_s and R_{sh}) from the I-V characteristics of PV cells/modules due to the transcendental nature of (3). For such a one-diode PV model, the existing identification methods in literature can be divided into the following two categories.

1.2.1. Deterministic Solution

The deterministic solution is an unique solution of the five unknown parameters (I_L, I_o, a, R_s and R_{sh}) from five independent equations. Usually, the four independent equations are chosen from the open circuit, short circuit and maximum power points at STC (1000 W/m^2, $T_c = 25°\text{C}$, $\text{AM} = 1.5$) as follows.

At short circuit (SC), $V = 0$:

$$I_{sc} = I_L - I_o\left(\mathrm{e}^{\frac{Rs\,Isc}{a}} - 1\right) - \frac{R_s I_{sc}}{R_{sh}}. \tag{4}$$

At open circuit (OC), $I = 0$:

$$I_L - I_o\left(\mathrm{e}^{\frac{Voc}{a}} - 1\right) - \frac{V_{oc}}{R_{sh}} = 0. \tag{5}$$

At maximum power point (MPP), $\mathrm{d}P/\mathrm{d}V = 0$:

$$I_{mpp} = I_L - I_o\left(\mathrm{e}^{\frac{Vmpp + Rs\,Impp}{a}} - 1\right) - \frac{V_{mpp} + R_s I_{mpp}}{R_{sh}}. \tag{6}$$

$$\left.\frac{\mathrm{d}IV}{\mathrm{d}V}\right|_{mpp} = -\frac{V_{mpp}}{R_s + \frac{1}{\frac{Io}{a}\mathrm{e}^{\frac{Vmpp+Impp\,Rs}{a}} + \frac{1}{R_{sh}}}} + I_{mpp} = 0. \tag{7}$$

As for the 5th independent equation, there are many options.

One way is to estimate one of the five parameters independently. For example, I_L can be estimated from the influence of the structure parameters of a silicon solar cell on photocurrent [8]. I_o is material independent and can be explicitly related to a solid state parameter, the $0K$ Debye temperature of the semiconductor [9]. a can be determined from the use of properties of special trans function theory (STFT) [10]. The estimation of R_s are well summarized in [11–15]. R_{sh} can be approximated by the reciprocal of slope at SC [16], i.e.,

$$R_{sh} \approx -\left.\frac{\mathrm{d}V}{\mathrm{d}I}\right|_{sc}. \tag{8}$$

For example, with equation (4)-(8), one-diode model parameters can be identified as [17]

$$\begin{aligned}
I_L &= I_{sc}\left(1 + \frac{R_s}{R_{sh}}\right) + I_o\left(\mathrm{e}^{\frac{Isc\,Rs}{a}} - 1\right), \\
I_o &= \left(I_{sc} - \frac{V_{oc}}{R_{sh}}\right)\mathrm{e}^{-\frac{Voc}{a}}, \\
a &= \frac{V_{mpp} + I_{mpp}R_{s0} - V_{oc}}{\ln\left(I_{sc} - \frac{V_{mpp}}{R_{sh}} - I_{mpp}\right) - \ln\left(I_{sc} - \frac{V_{oc}}{R_{sh}}\right) + \frac{I_{mpp}}{I_{sc} - \frac{V_{oc}}{R_{sh}}}}, \\
R_s &= R_{s0} - \frac{a}{I_0}\mathrm{e}^{-\frac{Voc}{a}},
\end{aligned}$$

where $R_{s0} = -\left.\mathrm{d}V/\mathrm{d}I\right|_{oc}$ is the reciprocal of slope at OC.

The other way is to apply one of (4)-(7) to non-STC conditions. For example, applying (5) to $T_c^* = T_c + \Delta T$ ($\Delta T \neq 0$) gives

$$I_L^* - I_o^*\left(\mathrm{e}^{\frac{V_{oc}^*}{a^*}} - 1\right) - \frac{V_{oc}^*}{R_{sh}^*} = 0. \tag{9}$$

In the case of no irradiance change, non-STC parameters are given by [2, 18]

$$I_L^* = I_L + \alpha_T \Delta T, \tag{10}$$

$$I_o^* = I_o\left(\frac{T_c^*}{T_c}\right)^3 \mathrm{e}^{\frac{Eg}{kTc} - \frac{E_g^*}{kT^*}}, \tag{11}$$

$$E_g^* = E_g(1 - 0.0002677\Delta T), \tag{12}$$

$$a^* = \frac{T_c^*}{T_c}a, \tag{13}$$

$$R_{sh}^* = R_{sh}, \tag{14}$$

$$V_{oc}^* = V_{oc} + \beta_T \Delta T, \tag{15}$$

where $E_g = 1.17 - 4.73 \times 10^{-4} T_c^2/(T_c + 636)$ is the band gap energy, α_T and β_T are the temperature coefficient of SC current and OC voltage, respectively. Substituting (10)-(15) into (9) yields the 5th independent equation as follows

$$I_L + \alpha_T \Delta T - I_o \left(\frac{T_c^*}{T_c}\right)^3 \mathrm{e}^{\frac{Eg}{kTc} - \frac{Eg(1-0.0002677\Delta T)}{kT^*}} \left(\mathrm{e}^{\frac{Voc+\beta_T \Delta T}{a} \frac{Tc}{T_c^*}} - 1\right) - \frac{V_{oc} + \beta_T \Delta T}{R_{sh}} = 0.$$

Different choices of non-STC equations yield different solutions for (I_L, I_o, a, R_s and R_{sh}), which can be found in [19–23].

No matter what the 5th equation is, a small variation in one parameter may lead to a large error in the other four parameters, due to the high sensitivity of the transcendental equation [24]. Even if there is no approximation in the 5th equation, there are no analytical solutions available due to the inherent nonlinearity. Usually, partial linearization has to be made to yield empirical formulas [25–29], which is a trade-off between simplicity and accuracy. Note that the greatest difficulty in solving (3) lies in its implicit format of I, i.e., I are both dependent and independent variable of the equation. Recent progress to overcome such difficulty is to apply the Lambert W function [30, 31] to (3), then the implicit format of I is converted to its equivalent explicit format as [18, 32]

$$I = \frac{R_{sh}(I_L + I_o) - V}{R_s + R_{sh}} - \frac{a}{R_s} W\left(\frac{I_o R_s R_{sh}}{a(R_s + R_{sh})} \mathrm{e}^{\frac{R_{sh}(V + Rs(I_L + Io))}{a(Rs + R_{sh})}}\right). \tag{16}$$

The benefit of (16) over (3) is that the former is not transcendental anymore, which makes it possible to find solutions to (4)-(7) by iterative algorithms.

1.2.2. Optimal Solution

Optimal solution employs nonlinear fitting procedures based on the minimization of deviations between modelled and measured I-V curves, in accordance with some metric function (usually least square) [33–36], e.g.,

$$\min f(I_L, I_o, a, R_s, R_{sh}) = \sum_{i=1}^{N} \left[I_i - \hat{I}_i(V_i, I_L, I_o, a, R_s, R_{sh})\right]^2,$$

where N is the number of data samples, $\hat{I}$ is the estimation of I with the optimal solution of I_L, I_o, a, R_s and R_{sh}. Iterative searching algorithms are usually used [37, 38], including Newton-Raphson [39], Levenberg-Marquardt [40], Gauss Siedal [16], and singular value decomposition [41], but their convergence and accuracy heavily depend on the initial values and are easily trapped in the local optimums. From different initial value guesses, such approaches can result in widely different parameter sets, all leading to satisfactory curve fitting [42]. Although a good match between estimation and measured data can be obtained, there is no guarantee that the estimated I-V curve would pass the SC, OC and MPP points.

To achieve the global optimum, soft computing techniques have to be used, which include genetic algorithm (GA) [43–46], particle swarm optimisation (PSO) [47–49], differential evolution (DE) [50–52], simulated annealing (SA) [53, 54] and artificial neural network (ANN) [55, 56]. But they are too complicated to be implemented and unsuitable for online calculation due to the heavy burden of computing.

Current trend of PV model identification is to combine the deterministic and optimal solutions, i.e.,employing both methods of solving algebraic equations and iterative searching [57–59]. With a single parameter fitting procedure, numerical solutions to (4)-(7) will be obtained by the empirical formulas or iterative algorithms. The drawbacks of the above two categories are mitigated in this way. With the help of Lambert W function as shown in (16), Laudani *et al.* further reduce the dimension of searching space from 5 to 2 by splitting the model parameters into two independent unknowns (a and R_s) and three dependent ones (I_L, I_o and R_{sh}). In this way, the burden of iterative searching is greatly relieved and it becomes easy to get a and R_s numerically or graphically. The review and comparison for the aforementioned all kinds of methods are well summarised in [60, 61].

This chapter opens a new angle to view the diode model from the systems perspective. Actually, one of the biggest application of Lambert W function is to solve differential equations, which is directly linked to the time-domain representation of a linear system. For example, the first-order linear system can be described as [62]

$$T\frac{\mathrm{d}y(t)}{\mathrm{d}t} + y(t) = u(t), \tag{17}$$

where T is the time constant of the system. The unit ramp ($u(t) = t$) response of (17) is given by,

$$y(t) = t + T(\mathrm{e}^{-\frac{t}{T}} - 1),$$

which has the same format as (3). This motivates us that the I-V curve governed by (3) can be viewed as the output of some linear system, and the model parameters can be linked to the coefficients of a linear differential equation. Using system identification methods available in the literature [63], PV model parameters can be easily identified by a simple linear least squares method.

2. Dynamic System Formulation

Firstly, we show how to link one-diode model to an equivalent linear system. Next, the same method is extended to the general case of multi-diode model.

2.1. One-Diode Model

Recall the I-V curve described by (3) with $m = 1$. Let $y = I$ and $x = V + R_sI$, (3) then becomes

$$y = I_L + I_o - I_o\mathrm{e}^{\frac{x}{a}} - \frac{x}{R_{sh}}. \tag{18}$$

Taking differential once on both sides of (18) gives

$$\frac{\mathrm{d}y}{\mathrm{d}x} = -\frac{I_o}{a}\mathrm{e}^{\frac{x}{a}} - \frac{1}{R_{sh}}. \tag{19}$$

Differentiating one more time for (19) gives

$$\frac{\mathrm{d}^2y}{\mathrm{d}x^2} = -\frac{I_o}{a^2}\mathrm{e}^{\frac{x}{a}}. \tag{20}$$

Eliminating $\mathrm{e}^{x/a}$ from (19) and (20) gives

$$a\frac{\mathrm{d}^2y}{\mathrm{d}x^2} - \frac{\mathrm{d}y}{\mathrm{d}x} = \frac{1}{R_{sh}}. \tag{21}$$

Let $t = x$ and $u(t) \equiv 1$, (21) is equivalent to

$$a\frac{\mathrm{d}^2y(t)}{\mathrm{d}t^2} - \frac{\mathrm{d}y(t)}{\mathrm{d}t} = \frac{u(t)}{R_{sh}}, \tag{22}$$

which is a standard differential equation representation of a second order linear system. t is the "time", $u(t)$ and $y(t)$ are the system "input" and "output", respectively. Since $u(t) \equiv 1$, $y(t)$ is the unit step response of the system in "time" domain. Taking Laplace transform, $F(s) = \mathcal{L}[f(t)] = \int_0^\infty \mathrm{e}^{-st} f(t)\mathrm{d}t$, on both sides of (22),

$$a[s^2Y(s) - sy(0) - y'(0)] - [sY(s) - y(0)] = \frac{U(s)}{R_{sh}}. \tag{23}$$

Utilize $sU(s) = 1$, and (23) is equivalent to

$$a\left[s^2Y(s) - s^2U(s)y(0) - sU(s)y'(0)\right] - [sY(s) - sU(s)y(0)] = \frac{1}{R_{sh}}U(s).$$

It follows from (18) that $y(0) = I_L$, $y'(0) = -I_o/a - 1/R_{sh}$, so the transfer function from $Y(s)$ to $U(s)$ is

$$\begin{aligned} G(s) := \frac{Y(s)}{U(s)} &= \frac{ay(0)s^2 + [ay'(0) - y(0)]s + \frac{1}{R_{sh}}}{as^2 - s} \\ &= \frac{aI_Ls^2 - (I_o + \frac{a}{R_{sh}} + I_L)s + \frac{1}{R_{sh}}}{as^2 - s}. \end{aligned} \tag{24}$$

The corresponding time domain differential equation is

$$a\frac{\mathrm{d}^2y(t)}{\mathrm{d}t^2} - \frac{\mathrm{d}y(t)}{\mathrm{d}t} = aI_L\frac{\mathrm{d}^2u(t)}{\mathrm{d}t^2} - \left(I_L + I_o + \frac{a}{R_{sh}}\right)\frac{\mathrm{d}u(t)}{\mathrm{d}t} + \frac{u(t)}{R_{sh}}. \tag{25}$$

It should be noted that (22) is different from (25) because of the non-zero initial conditions. In other words, (25) is the description of the same system of (22) but with zero initial conditions. This will facilitate the calculation of the integral-based identification proposed in Section 3

2.2. Multi-Diode Model

Similarly by letting $y = I$ and $x = V + R_sI$ in (3), it yields

$$y = I_L + \sum_{i=1}^{m} I_{o_i} - \sum_{i=1}^{m} I_{o_i}\mathrm{e}^{\frac{x}{a_i}} - \frac{x}{R_{sh}}. \tag{26}$$

Taking differential once on both sides of (26) gives

$$\frac{\mathrm{d}y}{\mathrm{d}x} = -\sum_{i=1}^{m} \frac{I_{o_i}}{a_i}\mathrm{e}^{\frac{x}{a_i}} - \frac{1}{R_{sh}}. \tag{27}$$

Differentiating (27) for k times, $k = 1, 2, \cdots, m$, yields

$$y^{(k+1)}(x) = -\sum_{i=1}^{m} \frac{I_{o_i}}{a_i^{k+1}} \mathrm{e}^{\frac{x}{a_i}}, \tag{28}$$

where $y^{(k)}(x) = \mathrm{d}^k y/\mathrm{d}x^k$. Rewrite (28) in matrix format,

$$\underbrace{\begin{bmatrix} y^{(2)}(x) \\ y^{(3)}(x) \\ \vdots \\ y^{(m+1)}(x) \end{bmatrix}}_{B} = \underbrace{\begin{bmatrix} a_1^{-1} & a_2^{-1} & \cdots & a_m^{-1} \\ a_1^{-2} & a_2^{-2} & \cdots & a_m^{-2} \\ \vdots & \vdots & \ddots & \vdots \\ a_1^{-m} & a_2^{-m} & \cdots & a_m^{-m} \end{bmatrix}}_{A} \begin{bmatrix} -\frac{I_{o_1}}{a_1}\mathrm{e}^{\frac{x}{a_1}} \\ -\frac{I_{o_2}}{a_2}\mathrm{e}^{\frac{x}{a_2}} \\ \vdots \\ -\frac{I_{om}}{a_m}\mathrm{e}^{\frac{x}{am}} \end{bmatrix}.$$

Since $a_k \neq 0$, A is a Vandermonde matrix with $\det(A) \neq 0$, so A^{-1} exists and

$$\left[-\frac{I_{o_1}}{a_1}\mathrm{e}^{\frac{x}{a_1}}, -\frac{I_{o_2}}{a_2}\mathrm{e}^{\frac{x}{a_2}}, \ldots - \frac{I_{o_m}}{a_m}\mathrm{e}^{\frac{x}{am}}\right]^T = A^{-1}B, \tag{29}$$

where $A^{-1} = [\xi_{i,j}] \in \mathbb{R}_{m\times m}$ with

$$\xi_{i,j} = \frac{\displaystyle\sum_{\substack{1\leq k_1<\cdots<k_{n-j}\leq n \\ k_1,\cdots,k_{n-j}\neq i}} (-1)^{j-1} a_{k_1}^{-1} \cdots a_{k_{n-j}}^{-1}}{\displaystyle a_i^{-1} \prod_{\substack{1\leq k\leq n \\ k\neq i}} \left(a_k^{-1} - a_i^{-1}\right)}. \tag{30}$$

Substituting (29) into (27) yields

$$y^{(1)}(x) - \sum_{j=1}^{m}\sum_{i=1}^{m} \xi_{i,j} y^{(j+1)}(x) = -\frac{1}{R_{sh}}. \tag{31}$$

Let $t = x$ and $u(t) \equiv 1$, (31) becomes the differential equation representation of an mth-order “dynamic” system:

$$y^{(1)}(t) - \sum_{j=1}^{m}\sum_{i=1}^{m} \xi_{i,j} y^{(j+1)}(t) = -\frac{u(t)}{R_{sh}}. \tag{32}$$

Taking Laplace transform for both sides of (32) yields

$$sY(s) - y(0) - \sum_{j=1}^{m}\sum_{i=1}^{m} \xi_{i,j} \left(s^{j+1}Y(s) - \sum_{k=1}^{j+1} s^{k-1} y^{(j+1-k)}(0)\right) = -\frac{U(s)}{R_{sh}}. \tag{33}$$

It follows from (26)-(28) that $y(0) = I_L$, $y^{(1)}(0) = -\sum_{i=1}^{m} I_{o_i}/a_i - 1/R_{sh}$, $y^{(k+1)}(0) = -\sum_{i=1}^{m} I_{o_i}/a_i^{k+1}$ for $k = 1, 2, \cdots, m$. Since $sU(s) = 1$, (33) becomes

$$sY(s) - I_L sU(s) - \sum_{j=1}^{m}\sum_{i=1}^{m} \xi_{i,j} \Bigg[s^{j+1}Y(s) - U(s)\times \\ \left(\sum_{k=1}^{j} s^k \sum_{i=1}^{m} \frac{-I_{o_i}}{a_i^{j+1-k}} - \frac{s^j}{R_{sh}} + I_L s^{j+1}\right)\Bigg] = -\frac{U(s)}{R_{sh}}.$$

The transfer function is $G(s) = Y(s)/U(s) = N/D$, where

$$D = \sum_{j=1}^{m} \sum_{i=1}^{m} \xi_{i,j} s^{j+1} - s,$$

$$N = \frac{1}{R_{sh}} - I_L s + \sum_{j=1}^{m} \sum_{i=1}^{m} \xi_{i,j} \left(I_L s^{j+1} - \frac{s^j}{R_{sh}} - \sum_{k=1}^{j} s^k \sum_{i=1}^{m} \frac{I_{o_i}}{a_i^{j+1-k}} \right).$$

The corresponding time domain differential equation with zero initial condition is

$$\begin{aligned} &\alpha_{m+1} y^{(m+1)}(t) + \cdots + \alpha_2 y^{(2)}(t) - y^{(1)}(t) \\ =&\beta_{m+1} u^{(m+1)}(t) + \cdots + \beta_1 u^{(1)}(t) + \frac{u(t)}{R_{sh}}, \end{aligned} \tag{34}$$

where for $j = 1, 2, \cdots, m$,

$$\alpha_1 = -1, \tag{35}$$

$$\alpha_{j+1} = \sum_{i=1}^{m} \xi_{i,j}, \tag{36}$$

$$\beta_j = \alpha_j I_L - \frac{\alpha_{j+1}}{R_{sh}} - \sum_{k=j}^{m} \sum_{i=1}^{m} \frac{\alpha_{k+1} I_{o_i}}{a_i^{k+1-j}}, \tag{37}$$

$$\beta_{m+1} = \alpha_{m+1} I_L. \tag{38}$$

In general, by introducing a virtual "time" of $t = x$, the static relationship between two variables y and x can be regarded as dynamics from the linear system governed by (34). Once α_i and β_i are determined from system identification, diode model parameters I_L, I_{o_i}, a_i and R_{sh} can be solved linearly from (36)-(37).

3. Integral-Based Linear Identification

For an integer $n \geq 1$, define the multiple integral as [63]

$$\int_{[T_1,T_2]}^{(n)} f(\tau) = \underbrace{\int_{T_1}^{T_2} \int_{T_1}^{\tau_n} \cdots \int_{T_1}^{\tau_2}}_{n} f(\tau_1) \mathrm{d}\tau_1 \mathrm{d}\tau_2 \cdots \mathrm{d}\tau_n. \tag{39}$$

3.1. One-Diode Model

Applying (39) to (25) for $T_1 = 0$, $T_2 = t$ and $n = 2$ gives

$$a y(t) - a I_L u(t) + \left(I_L + I_o + \frac{a}{R_{sh}} \right) \int_{[0,t]}^{(1)} u(\tau) - \frac{1}{R_{sh}} \int_{[0,t]}^{(2)} u(\tau) = \int_{[0,t]}^{(1)} y(\tau). \tag{40}$$

Let $\theta = [a, aI_L, I_L + I_o + \frac{a}{R_{sh}}, \frac{1}{R_{sh}}]^T$, $\phi(t) = [y(t), -u(t), \int_{[0,t]}^{(1)} u(\tau), -\int_{[0,t]}^{(2)} u(\tau)]^T$ and $\gamma(t) = \int_{[0,t]}^{(1)} y(\tau)$, (40) can be rewritten as the matrix format of $\phi^T(t)\theta = \gamma(t)$. Note that the matrix format holds for any $t_i \in [0,t]$, $i = 1,2,\cdots,N$, where N is the the number of data samples on the I-V curve. This actually casts an equation group of $\Phi\theta = \Gamma$ with $\Phi = [\phi(t_1), \phi(t_2), \cdots, \phi(t_N)]^T$ and $\Gamma = [\gamma(t_1), \gamma(t_2), \cdots, \gamma(t_N)]^T$. If $\Phi^T\Phi$ is nonsingular, the linear least square solution for θ is given by

$$\theta = \left(\Phi^T\Phi\right)^{-1}\Phi^T\Gamma, \tag{41}$$

which will minimise the square error of $(\Gamma - \Phi\theta)^T(\Gamma - \Phi\theta)$. Once θ is determined from (41), the parameters of one-diode model can be obtained by

$$\begin{aligned} a &= \theta_1, \\ I_L &= \frac{\theta_2}{\theta_1}, \\ I_o &= \theta_3 - \frac{\theta_2}{\theta_1} - \theta_1\theta_4, \\ R_{sh} &= \frac{1}{\theta_4}. \end{aligned}$$

3.2. Multi-Diode Model

Applying (39) to (34) for $T_1 = 0$, $T_2 = t$ and $n = m+1$,

$$\begin{aligned} &\alpha_{m+1}y(t) + \cdots + \alpha_2 \int_{[0,t]}^{(m-1)} y(\tau) - \int_{[0,t]}^{(m)} y(\tau) \\ =&\beta_{m+1}u(t) + \cdots + \beta_1 \int_{[0,t]}^{(m)} u(\tau) + \frac{1}{R_{sh}} \int_{[0,t]}^{(m+1)} u(\tau). \end{aligned}$$

Let $\theta = [\alpha_{m+1}, \cdots, \alpha_2, \beta_{m+1}, \cdots, \beta_1, \frac{1}{R_{sh}}]^T$, $\phi(t)$=$[y(t), \cdots, \int_{[o,t]}^{(m-1)} y(\tau), -u(t), \cdots, -\int_{[0,t]}^{(m+1)} u(\tau)]^T$, $\gamma(t) = \int_{[0,t]}^{(m)} y(\tau)$, θ and $\phi(t) \in \mathbb{R}_{(2m+2)\times 1}$, we have $\phi^T(t)\theta = \gamma(t)$. For $t_i \in [0,t]$, $i = 1,2,\cdots,N$, the equation group can be described by $\Phi\theta = \Gamma$ with $\Phi = [\phi(t_1), \phi(t_2), \cdots, \phi(t_N)]^T$ and $\Gamma = [\gamma(t_1), \gamma(t_2), \cdots, \gamma(t_N)]^T$. If $\Phi^T\Phi$ is nonsingular, the least square solution for θ will be

$$\theta = \left(\Phi^T\Phi\right)^{-1}\Phi^T\Gamma. \tag{42}$$

Once θ is determined from (42), $R_{sh} = 1/\theta_{2m+2}$ is immediately derived. It follows from (38) that $I_L = \beta_{m+1}/\alpha_{m+1} = \theta_{m+1}/\theta_1$.

a_i ($i = 1,2,\cdots,m$) will be derived in the following way. Rewriting (36) in matrix format gives

$$[\alpha_2, \cdots, \alpha_{m+1}] = \underbrace{[1, \cdots, 1]}_{m} A^{-1}.$$

Right-multiplying A for both sides gives

$$[\alpha_2, \cdots, \alpha_{m+1}] \begin{bmatrix} a_1^{-1} & \cdots & a_m^{-1} \\ \vdots & \ddots & \vdots \\ a_1^{-m} & \cdots & a_m^{-m} \end{bmatrix} = \underbrace{[1, \cdots, 1]}_{m},$$

which implies that $1/a_i$ are the roots of the following characteristic equation

$$\alpha_{m+1}\lambda^m + \alpha_m\lambda^{m-1} + \cdots + \alpha_2\lambda - 1 = 0. \tag{43}$$

Solving (43) for λ_i, and $a_i = 1/\lambda_i$, I_{o_i} $(i = 1, 2, \cdots, m)$ will be derived as follows. (37) can be rewritten as

$$\beta_j = \alpha_j I_L - \frac{\alpha_{j+1}}{R_{sh}} - \sum_{i=1}^{m} I_{o_i} \sum_{k=j}^{m} \frac{\alpha_{k+1}}{a_i^{k+1-j}}.$$

Rewriting further as matrix format,

$$\underbrace{\begin{bmatrix} \sum\limits_{k=1}^{m} \frac{\alpha_{k+1}}{a_1^k} & \sum\limits_{k=1}^{m} \frac{\alpha_{k+1}}{a_2^k} & \cdots & \sum\limits_{k=1}^{m} \frac{\alpha_{k+1}}{a_m^k} \\ \sum\limits_{k=2}^{m} \frac{\alpha_{k+1}}{a_1^{k-1}} & \sum\limits_{k=2}^{m} \frac{\alpha_{k+1}}{a_2^{k-1}} & \cdots & \sum\limits_{k=2}^{m} \frac{\alpha_{k+1}}{a_m^{k-1}} \\ \vdots & \vdots & \ddots & \vdots \\ \sum\limits_{k=m}^{m} \frac{\alpha_{k+1}}{a_1^{k+1-m}} & \sum\limits_{k=m}^{m} \frac{\alpha_{k+1}}{a_2^{k+1-m}} & \cdots & \sum\limits_{k=m}^{m} \frac{\alpha_{k+1}}{a_m^{k+1-m}} \end{bmatrix}}_{\Psi} \begin{bmatrix} I_{o_1} \\ I_{o_2} \\ \vdots \\ I_{om} \end{bmatrix} = - \underbrace{\begin{bmatrix} \beta_1 + I_L + \frac{\alpha_2}{R_{sh}} \\ \beta_2 - \alpha_2 I_L + \frac{\alpha_3}{R_{sh}} \\ \vdots \\ \beta_m - \alpha_m I_L + \frac{\alpha_{m+1}}{R_{sh}} \end{bmatrix}}_{\Xi}$$

Note from (43) that $\sum_{k=1}^{m} \alpha_{k+1}/a_i^k = 1$ for $i = 1, 2, \cdots, m$, Ψ can be simplified as

$$\Psi = \underbrace{\begin{bmatrix} 1 & 1 & \cdots & 1 \\ a_1 & a_2 & \cdots & a_m \\ \vdots & \vdots & \ddots & \vdots \\ a_1^{m-1} & a_2^{m-1} & \cdots & a_m^{m-1} \end{bmatrix}}_{\Psi^*} - \begin{bmatrix} 0 & \cdots & 0 \\ \alpha_2 & \cdots & \alpha_2 \\ \vdots & \ddots & \vdots \\ \sum\limits_{k=1}^{m-1} \alpha_{k+1} a_1^{m-1-k} & \cdots & \sum\limits_{k=1}^{m-1} \alpha_{k+1} a_m^{m-1-k} \end{bmatrix}.$$

This implies that after elementary row operations, Ψ is similar to Ψ^*, which is a Vandermonde matrix with $\det(\Psi^*) \neq 0$. Therefore, Ψ^{-1} exists (Ψ is full rank) and $[I_{o_1}, I_{o_2}, \cdots, I_{o_m}]^T = \Psi^{-1}\Xi$.

3.3. Nonsingularity of $\Phi^T\Phi$

The existence of the linear least square solution by (41) and (42) depends on the nonsingularity of $\Phi^T\Phi$, which is shown by the following lemma.

Lemma 3.1. $\Phi^T\Phi$ *is nonsingular if* $a_i \neq a_j$ *for* $i \neq j$, $i, j = 1, 2, \cdots, m$, *and the sampling number* $N \geq 2m + 2$.

Proof. Consider the general case of multi-diode model with

$$\Phi = [\phi(t_1), \phi(t_2), \cdots, \phi(t_N)]^T := [\Phi_1, \Phi_2],$$

$$\Phi_1 = \begin{bmatrix} y(t_1) & \int_{[0,t_1]}^{(1)} y(\tau) & \cdots & \int_{[0,t_1]}^{(m-1)} y(\tau) \\ y(t_2) & \int_{[0,t_2]}^{(1)} y(\tau) & \cdots & \int_{[0,t_2]}^{(m-1)} y(\tau) \\ \vdots & \vdots & \ddots & \vdots \\ y(t_N) & \int_{[0,t_N]}^{(1)} y(\tau) & \cdots & \int_{[0,t_N]}^{(m-1)} y(\tau) \end{bmatrix} := [\phi_{i,j}],$$

$$\Phi_2 = - \begin{bmatrix} u(t_1) & \int_{[0,t_1]}^{(1)} u(\tau) & \cdots & \int_{[0,t_1]}^{(m+1)} u(\tau) \\ u(t_2) & \int_{[0,t_2]}^{(1)} u(\tau) & \cdots & \int_{[0,t_2]}^{(m+1)} u(\tau) \\ \vdots & \vdots & \ddots & \vdots \\ u(t_N) & \int_{[0,t_N]}^{(1)} u(\tau) & \cdots & \int_{[0,t_N]}^{(m+1)} u(\tau) \end{bmatrix} =: [\varphi_{i,l}].$$

Recall from (26) that

$$y(t) = I_L + \sum_{i=1}^{m} I_{o_i} - \sum_{i=1}^{m} I_{o_i} \mathrm{e}^{\frac{t}{a_i}} - \frac{t}{R_{sh}},$$

and $u(t) \equiv 1$ by the definition. For $i = 1, 2, \cdots, N$,

$$\phi_{i,j} = \int_{[0,t_i]}^{(j-1)} y(\tau) = \frac{I_L + \sum\limits_{i=1}^{m} I_{o_i}}{(j-1)!} t_i^{j-1} - \frac{t_i^j}{j! R_{sh}} + \sum_{k=0}^{j-2} \sum_{l=1}^{m} I_{o_l} a_l^{j-k-1} \frac{t_i^k}{k!} - \sum_{k=1}^{j} I_{o_k} a_k^{j-1} \mathrm{e}^{\frac{t_i}{a_k}},$$
$$\varphi_{i,l} = -\int_{[0,t_i]}^{(l-1)} u(\tau) = -\frac{1}{j!} t_i^l,$$

where $j = 1, 2, \cdots, m$ and $l = 1, 2, \cdots, m+2$. After elementary column operations for Φ, $\Phi_1 \to \tilde{\Phi}_1 := [\tilde{\phi}_{i,j}]$ with

$$\tilde{\phi}_{i,j} = \sum_{k=1}^{j} I_{o_k} a_k^{j-1} \mathrm{e}^{\frac{t_i}{a_k}}.$$

In matrix format,

$$\tilde{\Phi}_1 = \underbrace{\begin{bmatrix} \mathrm{e}^{\frac{t_1}{a_1}} & \mathrm{e}^{\frac{t_1}{a_2}} & \cdots & \mathrm{e}^{\frac{t_1}{am}} \\ \mathrm{e}^{\frac{t_2}{a_1}} & \mathrm{e}^{\frac{t_2}{a_2}} & \cdots & \mathrm{e}^{\frac{t_2}{am}} \\ \vdots & \vdots & \ddots & \vdots \\ \mathrm{e}^{\frac{t_N}{a_1}} & \mathrm{e}^{\frac{t_N}{a_2}} & \cdots & \mathrm{e}^{\frac{t_N}{am}} \end{bmatrix}}_{E} \underbrace{\begin{bmatrix} I_{o_1} & & & \\ & I_{o_2} & & \\ & & \ddots & \\ & & & I_{o_m} \end{bmatrix}}_{\Lambda} \underbrace{\begin{bmatrix} 1 & a_1 & \cdots & a_1^{m-1} \\ 1 & a_2 & \cdots & a_2^{m-1} \\ \vdots & \vdots & \ddots & \vdots \\ 1 & a_m & \cdots & a_m^{m-1} \end{bmatrix}}_{V^*}.$$

Since Λ is diagonal and V^* is a standard Vandermonde matrix, $\mathrm{rank}(\Lambda) = \mathrm{rank}(V^*) = m$. If $t_2 - t_1 = t_3 - t_2 = \cdots = t_m - t_{m-1} = T_s > 0$, as $N \geq 2m+2$, the first m row of E

$$E_m = \begin{bmatrix} 1 & 1 & \cdots & 1 \\ \mathrm{e}^{\frac{Ts}{a_1}} & \mathrm{e}^{\frac{Ts}{a_2}} & \cdots & \mathrm{e}^{\frac{Ts}{am}} \\ \vdots & \vdots & \ddots & \vdots \\ (\mathrm{e}^{\frac{Ts}{a_1}})^{n-1} & (\mathrm{e}^{\frac{Ts}{a_2}})^{n-1} & \cdots & (\mathrm{e}^{\frac{Ts}{am}})^{m-1} \end{bmatrix} \begin{bmatrix} \mathrm{e}^{\frac{t_1}{a_1}} & & & \\ & \mathrm{e}^{\frac{t_1}{a_2}} & & \\ & & \ddots & \\ & & & \mathrm{e}^{\frac{t_1}{am}} \end{bmatrix},$$

so $\operatorname{rank}(E) = \operatorname{rank}(E_m) = m$. Otherwise, it is always possible to find some ΔT such that $t_i = n_i \Delta T$, $n_i \in \mathbb{N}$ for $i = 1, 2, \cdots, m$. Construct matrix

$$E^* = \begin{bmatrix} 1 & 1 & \cdots & 1 \\ e^{\frac{\Delta T}{a_1}} & e^{\frac{\Delta T}{a_2}} & \cdots & e^{\frac{\Delta T}{am}} \\ \vdots & \vdots & \ddots & \vdots \\ e^{\frac{nm\Delta T}{a_1}} & e^{\frac{nm\Delta T}{a_2}} & \cdots & e^{\frac{nm\Delta T}{am}} \end{bmatrix} \in \mathbb{R}_{n_m \times n},$$

and E_m is sub-matrix of E^*. Since E^* is a Vandermonde matrix with full column rank, $\operatorname{rank}(E) = \operatorname{rank}(E_m) = \operatorname{rank}(E^*) = m$. So, Φ_1 is full column rank, i.e., $\operatorname{rank}(\Phi_1) = m$.

$$\Phi_2 = \underbrace{\begin{bmatrix} t_1 & t_1^2 & \cdots & t_1^{m+2} \\ t_2 & t_2^2 & \cdots & t_2^{m+2} \\ \vdots & \vdots & \ddots & \vdots \\ t_N & t_N^2 & \cdots & t_N^{m+2} \end{bmatrix}}_{V_2} \begin{bmatrix} -1 & & & \\ & \ddots & & \\ & & \frac{-1}{(m+1)!} & \\ & & & \frac{-1}{(m+2)!} \end{bmatrix}$$

As $N \geq 2m + 2$, the first $m + 2$ row of V_2 is a Vandermonde matrix, so $\operatorname{rank}(\Phi_2) = \operatorname{rank}(V_2) = m + 2$, i.e., Φ_2 is full column rank. Since $\Phi = [\Phi_1, \Phi_2]$ with the full column rank of both Φ_1 and Φ_2, Φ is also full column rank. $N \geq 2m + 2$ implies that the row number of Φ is no less than the column number. So, $\operatorname{rank}(\Phi) = 2m + 2$ and $\Phi^T\Phi$ is full rank, i.e., $(\Phi^T\Phi)^{-1}$ exists. □

3.4. Calculation of Multiple Integrals

In practice, the integral shown as (39) is numerically estimated by rectangular or trapezoidal integration. For example, suppose there are N samples at $t_1, t_2, \cdots, t_N$, the rectangular integration gives

$$\begin{aligned} \int_{[t_1,t_i]}^{(1)} f(\tau) &= \int_{t_1}^{t_i} f(\tau_1) \mathrm{d}\tau_1 \approx \sum_{k=1}^{i-1} f(k)(t_{k+1} - t_k) := f_1(i), \\ \int_{[t_1,t_i]}^{(2)} f(\tau) &\approx \sum_{k=1}^{i-1} f_1(k)(t_{k+1} - t_k) := f_2(i), \\ &\vdots \\ \int_{[t_1,t_i]}^{(n)} f(\tau) &\approx \sum_{k=1}^{i-1} f_{n-1}(k)(t_{k+1} - t_k) := f_n(i). \end{aligned}$$

for $i = 1, 2, \cdots, N$. The more number of samples, f_i, the more accurate the estimation to the multiple integrals will be.

3.5. Determination of R_s

To calculate θ from (41) or (42), Φ and Γ must be known. As both of them are integrals to t, t must be known as well. Since $t = V + R_s I$, R_s must be determined before applying integrals. It is clear to see that if R_s is bigger than its real value, t will increase so that the whole I-V curve will move to the right and the error between the real and estimated I-V curves will be positive; If R_s decreases, the whole I-V curve will move to the left and the error between the real and estimated I-V curves will be negative. Thus, R_s can be used as a tuning parameter such that the root mean square error (RMSE) is minimised.

It derives from (3) that

$$-\frac{1}{\left.\frac{\mathrm{d}I}{\mathrm{d}V}\right|_{oc}} = R_s + \frac{1}{\sum\limits_{i=1}^{m} \frac{I_{o_i}}{a_i} \mathrm{e}^{\frac{Voc}{a_i}} + \frac{1}{R_{sh}}} > R_s,$$

which implies the upper bound of R_s, i.e., $R_s^{upp} = -1/\left.\frac{\mathrm{d}I}{\mathrm{d}V}\right|_{oc}$. The lower bound of R_s can be zero at first, i.e., $R_s^{low} = 0$. With such a band of $R_s \in [R_s^{low}, R_s^{upp}]$, binary search algorithm is applied to determine R_s in the following way:

Step 1. Arbitrarily choose R_s from $[R_s^{low}, R_s^{upp}]$ and calculate $\hat{a}_i$, $\hat{I}_L$, $\hat{I}_{o_i}$ and $\hat{R}_{sh}$ from the proposed linear least square (41) or (42);

Step 2. Calculate from (3) that

$$\hat{y}(t) = \hat{I}_L - \sum_{i=1}^{m} \hat{I}_{o_i} \left(\mathrm{e}^{\frac{V+RsI}{\hat{a_i}}} - 1 \right) - \frac{V + R_s I}{\hat{R}_{sh}},$$

and $RMSE = \sqrt{\sum_{i=1}^{N} \left[\hat{y}(t_i) - y(t_i)\right]^2 / N}$.

Step 3. Calculate $ERR = \sum_{i=1}^{N} [\hat{y}(t_i) - y(t_i)]$. If $ERR > 0$, adjust $R_s = (R_s + R_s^{low})/2$. Otherwise, adjust $R_s = (R_s + R_s^{upp})/2$.

Step 4. Update R_s^{upp} and R_s^{low} according to the sign of ERR. If $ERR > 0$, $R_s^{upp} = R_s$, otherwise, $R_s^{low} = R_s$.

Step 5. If $RMSE$ is less than some tolerance or the iterative cycle reaches some preset number, stop the searching. Otherwise, update R_s^{upp} and R_s^{low} according to the sign of ERR and go back to **Step 2**. The flowchart of the binary searching algorithm is shown in Figure 3.

3.6. Robustness Enhancement

From the viewpoint of control theory, the transfer function (24) has a pole of $s = 1/a > 0$, which implies the system (25) is unstable. This is also true for the general case of multi-diode model. Identification for unstable system is not preferred because the convergence of the proposed algorithm might be sensitive to the accuracy of the integral calculation in such a case. To improve the robustness of the proposed algorithm, $\tilde{V}$ is introduced to yield a stable system.

In case of one-diode model, let $V = V_{oc} - \tilde{V}$, $0 \leq \tilde{V} \leq V_{oc}$, and $\tilde{x} = \tilde{V} - R_s I$, thus

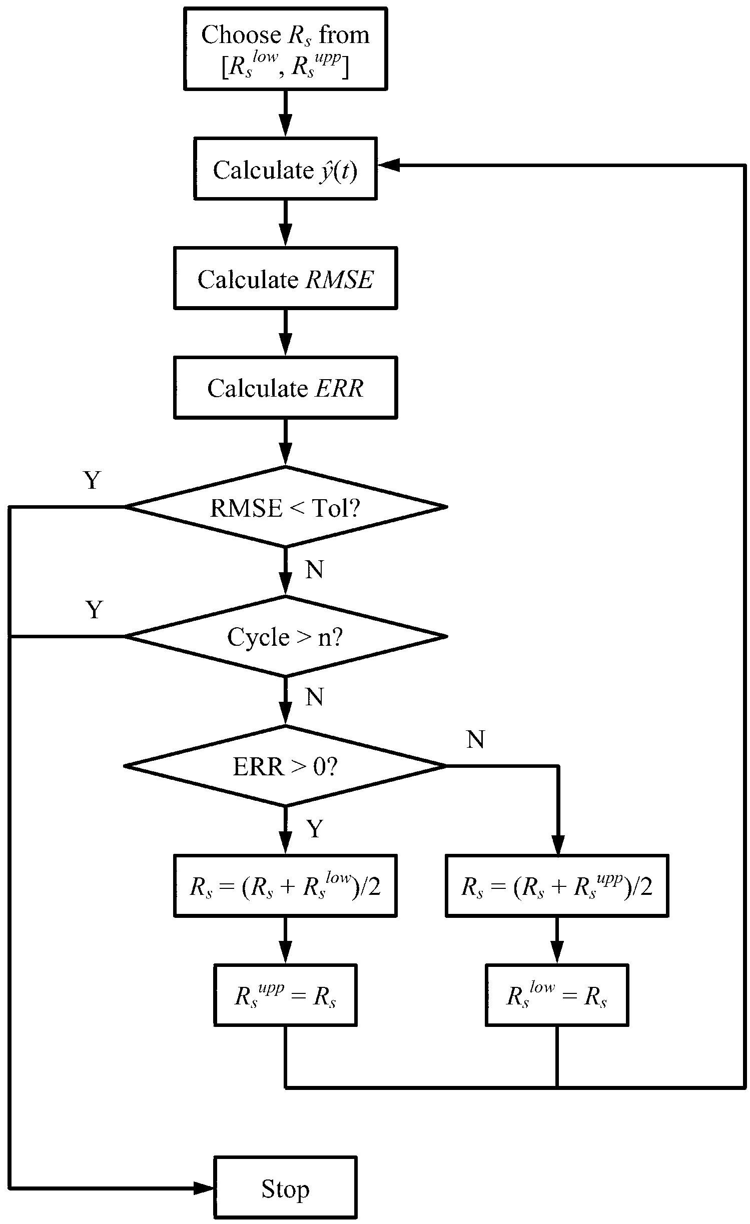

Figure 3. Flowchart of the binary searching algorithm.

$x = V + R_sI = V_{oc} - (\tilde{V} - R_sI) = V_{oc} - \tilde{x}$. It follows from (18)-(20) that

$$y = I_L + I_o - \frac{V_{oc}}{R_{sh}} - I_o e^{\frac{V_{oc}}{a}} e^{-\frac{\tilde{x}}{a}} + \frac{\tilde{x}}{R_{sh}},$$
$$\frac{\mathrm{d}y}{\mathrm{d}\tilde{x}} = \frac{I_o}{a} e^{\frac{V_{oc}}{a}} e^{-\frac{\tilde{x}}{a}} + \frac{1}{R_{sh}},$$
$$\frac{\mathrm{d}^2 y}{\mathrm{d}\tilde{x}^2} = -\frac{I_o}{a^2} e^{\frac{V_{oc}}{a}} e^{-\frac{\tilde{x}}{a}}.$$

Let $t = \tilde{x}$ and $u(t) \equiv 1$, by eliminating $\mathrm{e}^{-\tilde{x}/a}$ it gives

$$a\frac{\mathrm{d}^2 y(t)}{\mathrm{d}t^2} + \frac{\mathrm{d}y(t)}{\mathrm{d}t} = \frac{u(t)}{R_{sh}}.$$

The corresponding transfer function is

$$G(s) = \frac{Y(s)}{U(s)} = \frac{ay(0)s^2 + [ay'(0) + y(0)]s + \frac{1}{R_{sh}}}{as^2 + s},$$

where $y(0) = I_L - I_o(\mathrm{e}^{V_{oc}/a} - 1) - V_{oc}/R_{sh}$, $y'(0) = I_o\mathrm{e}^{V_{oc}/a}/a + 1/R_{sh}$. In this way, the unstable pole $s = 1/a > 0$ becomes stable as $s = -1/a < 0$.

The remaining procedures are the same as aforementioned. Let $\gamma(t) = -\int_{[0,t]}^{(1)} y(\tau)$, $\phi(t) = \left[y(t), -u(t), -\int_{[0,t]}^{(1)} u(\tau), -\int_{[0,t]}^{(2)} u(\tau)\right]^T$, and

$$\theta = \begin{bmatrix} a \\ aI_L - aI_o(\mathrm{e}^{\frac{V_{oc}}{a}} - 1) - \frac{aV_{oc}}{R_{sh}} \\ I_L + I_o - \frac{V_{oc} - a}{R_{sh}} \\ \frac{1}{R_{sh}} \end{bmatrix},$$

the linear least square solution is $\theta = \left(\Phi^T\Phi\right)^{-1}\Phi^T\Gamma$ with $\Phi = [\phi(t_1), \phi(t_2), \cdots, \phi(t_N)]^T$ and $\Gamma = [\gamma(t_1), \gamma(t_2), \cdots, \gamma(t_N)]^T$. Once θ is determined, the parameters of one-diode model are obtained by

$$\begin{aligned} a &= \theta_1, \\ I_L &= \frac{\theta_2}{\theta_1} + \left(\theta_3 - \frac{\theta_2}{\theta_1} - \theta_1\theta_4\right)\left(1 - \mathrm{e}^{-\frac{V_{oc}}{\theta_1}}\right) + V_{oc}\theta_4, \\ I_o &= \frac{\theta_3 - \frac{\theta_2}{\theta_1} - \theta_1\theta_4}{\mathrm{e}^{\frac{V_{oc}}{\theta_1}}}, \\ R_{sh} &= \frac{1}{\theta_4}. \end{aligned}$$

In the case of a multi-diode model, with the same transform of $x = V_{oc} - \tilde{x}$, (26) becomes

$$y = I_L + \sum_{i=1}^{m} I_{o_i} - \sum_{i=1}^{m} I_{o_i}\mathrm{e}^{\frac{V_{oc}}{a_i}}\mathrm{e}^{-\frac{\tilde{x}}{a_i}} - \frac{V_{oc}}{R_{sh}} + \frac{\tilde{x}}{R_{sh}}. \tag{44}$$

Let $\tilde{a}_i = -a_i$, $\tilde{I}_L = I_L + \sum_{i=1}^{m} I_{o_i}(1 - \mathrm{e}^{V_{oc}/a_i}) - V_{oc}/R_{sh}$, $\tilde{I}_{o_i} = I_{o_i}\mathrm{e}^{V_{oc}/a_i}$, $\tilde{R}_{sh} = -R_{sh}$, and (44) is equivalent to

$$y = \tilde{I}_L + \sum_{i=1}^{m} \tilde{I}_{o_i} - \sum_{i=1}^{m} \tilde{I}_{o_i}\mathrm{e}^{\frac{\tilde{x}}{\tilde{a}_i}} - \frac{\tilde{x}}{\tilde{R}_{sh}},$$

which has the same format as (26). This means that all the derivation aforementioned are applicable to the parameter set $\{\tilde{a}_i, \tilde{I}_L, \tilde{I}_{o_i}, \tilde{R}_{sh}\}$. Once they are determined, the parameter set $\{a_i, I_L, I_{o_i}, R_{sh}\}$ is derived immediately by

$$
\begin{aligned}
a_i &= -\tilde{a}_i,\\
R_{sh} &= -\tilde{R}_{sh},\\
I_{o_i} &= \tilde{I}_{o_i} \mathrm{e}^{-\frac{Voc}{a_i}},\\
I_L &= \tilde{I}_L - \sum_{i=1}^{m} I_{o_i}\left(1 - \mathrm{e}^{\frac{Voc}{a_i}}\right) + \frac{V_{oc}}{R_{sh}}.
\end{aligned}
$$

4. Validation

4.1. Indoor Flash Test

The I-V characteristics of full-sized commercial modules were measured indoor by a pulsed solar simulator (PASAN IIIB) with a constant illumination intensity plateau of about $12ms$ used. The data acquisition, which requires about $10ms$, occurs during the plateau period, whereby the light intensity varies by less than $\pm 1\%$. The intensity of the solar simulator is calibrated with a c-Si reference cell certified by Fraunhofer ISE. The overall uncertainty of module power measurement is within $\pm 2\%$.

Consider the I-V characteristic of a crystalline PV module from the indoor flash test under STC ($1000W/m^2$, $25°C$, $\mathrm{AM} = 1.5$) is shown in Figure 4. Both one-diode and two-diode models are considered for this case study.

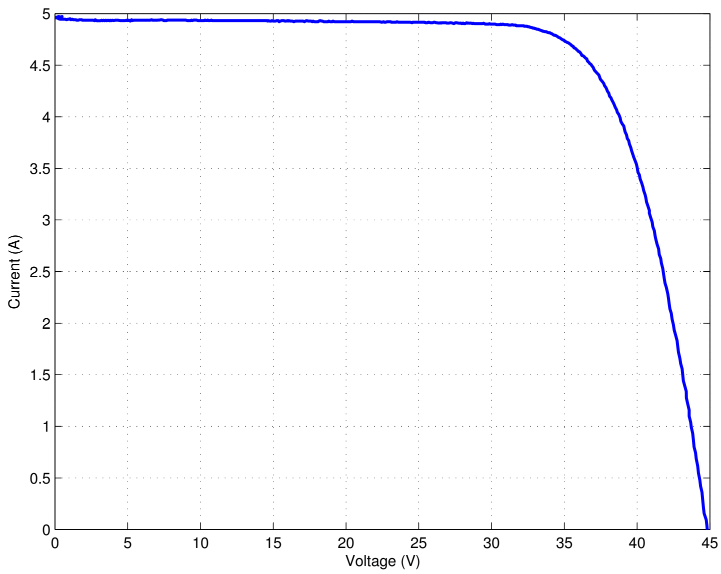

Figure 4. The I-V characteristic of a crystalline PV module.

4.1.1. One-Diode Model

Firstly, use the last 10 points at OC to derive a linear fitting: $I = kV + p$, where $k = -0.9131$. $R_s^{upp} \approx -1/k = 1.0952$. $R_s^{low} = 0$. Arbitrarily choose $R_s \in [R_s^{low}, R_s^{upp}]$, e.g., $R_s = 1.0952$, and follow the proposed integral-based linear identification presented in Section 3.1, R_s converges to $R_s = 0.655$ after about 30 steps with the proposed binary searching, as shown in Figure 6. Multiple integrals from (39) are estimated by the numerical integration presented in Section 3.4. It follows from (41) that $\theta_1 = 1.9891$, $\theta_2 = 9.8295$, $\theta_3 = 4.9434$, $\theta_4 = 8.9631 \times 10^{-4}$. Thus,

$$\begin{aligned}
a &= \theta_1 = 1.9891 \text{ (V)},\\
I_L &= \frac{\theta_2}{\theta_1} = 4.9416 \text{ (A)},\\
I_o &= \theta_3 - \frac{\theta_2}{\theta_1} - \theta_1\theta_4 = 4.1785 \times 10^{-9} \text{ (A)},\\
R_{sh} &= \frac{1}{\theta_4} = 1.1157 \times 10^3 \ (\Omega).
\end{aligned}$$

The comparison between the I-V curves from the real measurement and the one-code model is shown in Figure 5, where the average absolute error $\bar{E} = 1/N \sum_{i=1}^{N} |ERR| = 0.0085$. The $RMSE$ is shown in Figure 6, which converges to 1.67% at last after 35 steps with $\mathrm{Tol} = 2\%$.

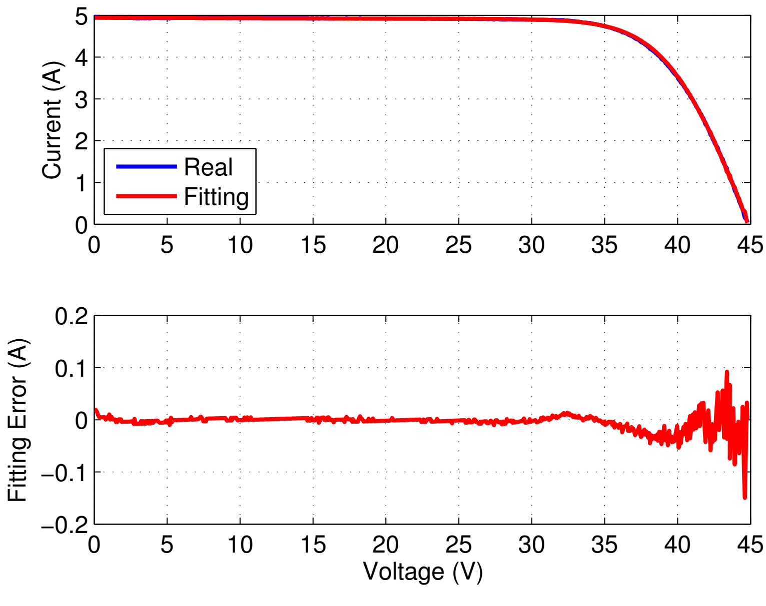

Figure 5. Accuracy of the proposed method for c-Si module.

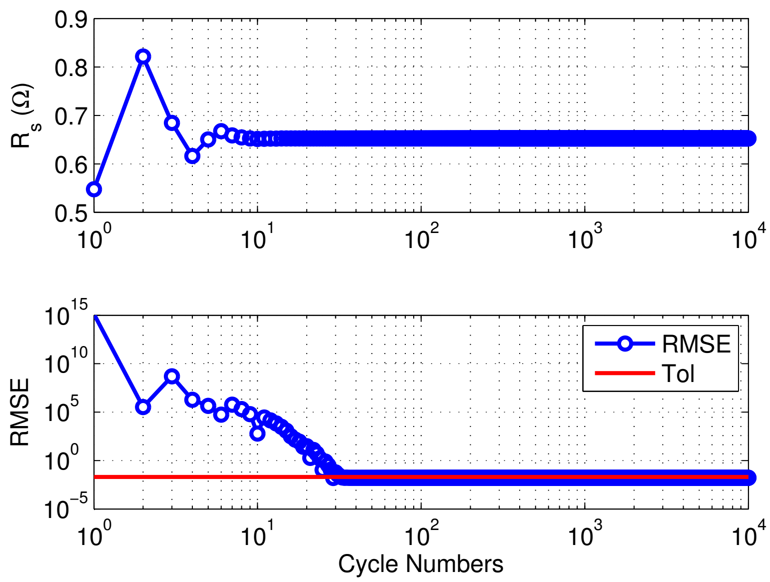

Figure 6. Convergence of R_s and $RMSE$ for c-Si module.

4.1.2. Two-Diode Model

It is clear to see from Figure 5 that one-diode model is good enough to represent the whole I-V curve accurately. This implies that if two-diode model is applied, $I_{o_2} \rightarrow 0$, which will cause a singular matrix in the identification of Section 3.2 To avoid such a potential problem, robustness enhancement discussed in Section 3.6 will be applied. With $m = 2$, (44) becomes

$$y = I_L + I_{o_1}\left(1 - \mathrm{e}^{\frac{Voc-\tilde{x}}{a_1}}\right) + I_{o_2}\left(1 - \mathrm{e}^{\frac{Voc-\tilde{x}}{a_2}}\right) - \frac{V_{oc} - \tilde{x}}{R_{sh}},$$

where $\tilde{x} = \tilde{V} - R_s I$, $\tilde{V} = V_{oc} - V$. And its multiple differentials are

$$\frac{\mathrm{d}y}{\mathrm{d}\tilde{x}} = \frac{I_{o_1}}{a_1}\mathrm{e}^{\frac{Voc-\tilde{x}}{a_1}} + \frac{I_{o_2}}{a_2}\mathrm{e}^{\frac{Voc-\tilde{x}}{a_2}} + \frac{1}{R_{sh}}, \tag{45}$$

$$\frac{\mathrm{d}^2y}{\mathrm{d}\tilde{x}^2} = -\frac{I_{o_1}}{a_1^2}\mathrm{e}^{\frac{Voc-\tilde{x}}{a_1}} - \frac{I_{o_2}}{a_2^2}\mathrm{e}^{\frac{Voc-\tilde{x}}{a_2}}, \tag{46}$$

$$\frac{\mathrm{d}^3y}{\mathrm{d}\tilde{x}^3} = \frac{I_{o_1}}{a_1^3}\mathrm{e}^{\frac{Voc-\tilde{x}}{a_1}} + \frac{I_{o_2}}{a_2^3}\mathrm{e}^{\frac{Voc-\tilde{x}}{a_2}}. \tag{47}$$

(46) and (47) in matrix format are

$$\begin{bmatrix} \frac{\mathrm{d}^2y}{\mathrm{d}\tilde{x}^2} \\ \frac{\mathrm{d}^3y}{\mathrm{d}\tilde{x}^3} \end{bmatrix} = \begin{bmatrix} -\frac{I_{o_1}}{a_1^2} & -\frac{I_{o_2}}{a_2^2} \\ \frac{I_{o_1}}{a_1^3} & \frac{I_{o_2}}{a_2^3} \end{bmatrix} \begin{bmatrix} \mathrm{e}^{\frac{Voc-\tilde{x}}{a_1}} \\ \mathrm{e}^{\frac{Voc-\tilde{x}}{a_2}} \end{bmatrix}.$$

Thus,

$$\begin{bmatrix} \mathrm{e}^{\frac{Voc-\tilde{x}}{a_1}} \\ \mathrm{e}^{\frac{Voc-\tilde{x}}{a_2}} \end{bmatrix} = \begin{bmatrix} -\dfrac{I_{o_1}}{a_1^2} & -\dfrac{I_{o_2}}{a_2^2} \\ \dfrac{I_{o_1}}{a_1^3} & \dfrac{I_{o_2}}{a_2^3} \end{bmatrix}^{-1} \begin{bmatrix} \dfrac{\mathrm{d}^2 y}{\mathrm{d}\tilde{x}^2} \\ \dfrac{\mathrm{d}^3 y}{\mathrm{d}\tilde{x}^3} \end{bmatrix}$$
$$= \begin{bmatrix} \dfrac{a_1^3}{I_{o_1}(a_2-a_1)} & \dfrac{a_1^3 a_2}{I_{o_1}(a_2-a_1)} \\ -\dfrac{a_2^3}{I_{o_2}(a_2-a_1)} & -\dfrac{a_1 a_2^3}{I_{o_2}(a_2-a_1)} \end{bmatrix} \begin{bmatrix} \dfrac{\mathrm{d}^2 y}{\mathrm{d}\tilde{x}^2} \\ \dfrac{\mathrm{d}^3 y}{\mathrm{d}\tilde{x}^3} \end{bmatrix}.$$

Substitute it into (45), it yields

$$a_1 a_2 \frac{\mathrm{d}^3 y(t)}{\mathrm{d}t^3} + (a_1+a_2)\frac{\mathrm{d}^2 y(t)}{\mathrm{d}t^2} + \frac{\mathrm{d}y(t)}{\mathrm{d}t} = \frac{u(t)}{R_{sh}}, \tag{48}$$

where $t = \tilde{x}$ and $u(t) \equiv 0$. After Laplace transform, (48) becomes

$$a_1 a_2 \left[s^3 Y(s) - y''(0) - sy'(0) - s^2 y(0)\right] + (a_1+a_2)\left[s^2 Y(s) - y'(0) - sy(0)\right]$$
$$+ [sY(s) - y(0)] = \frac{U(s)}{R_{sh}}, \tag{49}$$

where

$$y(0) = I_L + I_{o_1}\left(1 - \mathrm{e}^{\frac{Voc}{a_1}}\right) + I_{o_2}\left(1 - \mathrm{e}^{\frac{Voc}{a_2}}\right) - \frac{V_{oc}}{R_{sh}}, \tag{50}$$
$$y'(0) = \frac{I_{o_1}}{a_1}\mathrm{e}^{\frac{Voc}{a_1}} + \frac{I_{o_2}}{a_2}\mathrm{e}^{\frac{Voc}{a_2}} + \frac{1}{R_{sh}}, \tag{51}$$
$$y''(0) = -\frac{I_{o_1}}{a_1^2}\mathrm{e}^{\frac{Voc}{a_1}} - \frac{I_{o_2}}{a_2^2}\mathrm{e}^{\frac{Voc}{a_2}}. \tag{52}$$

Utilize $sU(s) = 1$, and (49) is equivalent to

$$a_1 a_2 s^3 Y(s) + (a_1+a_2)s^2 Y(s) - a_1 a_2 y(0) s^3 U(s) - \left[a_1 a_2 y'(0) + (a_1+a_2)y(0)\right] s^2 U(s)$$
$$-\frac{U(s)}{R_{sh}} - \left[a_1 a_2 y''(0) + (a_1+a_2)y'(0) + y(0)\right] sU(s) = -sY(s).$$

Therefore, the differential equation representation with zero initial conditions are

$$a_1 a_2 \frac{\mathrm{d}^3 y(t)}{\mathrm{d}t^3} + (a_1+a_2)\frac{\mathrm{d}^2 y(t)}{\mathrm{d}t^2} - a_1 a_2 y(0)\frac{\mathrm{d}^3 u(t)}{\mathrm{d}t^3} - \left[a_1 a_2 y'(0) + (a_1+a_2)y(0)\right]\frac{\mathrm{d}^2 u(t)}{\mathrm{d}t^2}$$
$$-\frac{u(t)}{R_{sh}} - \left[a_1 a_2 y''(0) + (a_1+a_2)y'(0) + y(0)\right]\frac{\mathrm{d}u(t)}{\mathrm{d}t} = -\frac{\mathrm{d}y(t)}{\mathrm{d}t}. \tag{53}$$

Applying triple integral (39) (with $n = 3$) to (53), we have

$$a_1 a_2 y(t) + (a_1+a_2)\int_{[0,t]}^{(1)} y(\tau) - a_1 a_2 y(0) u(t) - \left[a_1 a_2 y'(0) + (a_1+a_2)y(0)\right]\int_{[0,t]}^{(1)} u(\tau)$$
$$-\frac{1}{R_{sh}}\int_{[0,t]}^{(3)} u(\tau) - \left[a_1 a_2 y''(0) + (a_1+a_2)y'(0) + y(0)\right]\int_{[0,t]}^{(2)} u(\tau) = -\int_{[0,t]}^{(2)} y(\tau). \tag{54}$$

Let $\phi(t) = [y(t), \int_{[0,t]}^{(1)} y(\tau), -u(t), -\int_{[0,t]}^{(1)} u(\tau), -\int_{[0,t]}^{(2)} u(\tau), -\int_{[0,t]}^{(3)} u(\tau)]^T$,

$$\theta := \begin{bmatrix} \theta_1 \\ \theta_2 \\ \theta_3 \\ \theta_4 \\ \theta_5 \\ \theta_6 \end{bmatrix} = \begin{bmatrix} a_1 a_2 \\ a_1 + a_2 \\ \theta_1 y(0) \\ \theta_1 y'(0) + \theta_2 y(0) \\ \theta_1 y''(0) + \theta_2 y'(0) + y(0) \\ 1/R_{sh} \end{bmatrix}, \tag{55}$$

and $\gamma(t) = -\int_{[0,t]}^{(2)} y(\tau)$, then (54) can be rewritten in matrix format of $\phi(t)^T\theta = \gamma(t)$. The linear least solution to θ is given by (42). Immediately, $a_{1,2} = (\theta_2 \pm \sqrt{\theta_2^2 - 4\theta_1})/2$, $R_{sh} = 1/\theta_6$, and

$$\begin{bmatrix} \theta_3 \\ \theta_4 \\ \theta_5 \end{bmatrix} = \begin{bmatrix} \theta_1 & 0 & 0 \\ \theta_2 & \theta_1 & 0 \\ 1 & \theta_2 & \theta_1 \end{bmatrix} \begin{bmatrix} y(0) \\ y'(0) \\ y''(0) \end{bmatrix}.$$

Therefore,

$$\begin{bmatrix} y(0) \\ y'(0) \\ y''(0) \end{bmatrix} = \begin{bmatrix} \theta_1 & 0 & 0 \\ \theta_2 & \theta_1 & 0 \\ 1 & \theta_2 & \theta_1 \end{bmatrix}^{-1} \begin{bmatrix} \theta_3 \\ \theta_4 \\ \theta_5 \end{bmatrix}.$$

It follows from (50)-(52) that

$$\begin{bmatrix} y(0) + V_{oc}/R_{sh} \\ y'(0) - 1/R_{sh} \\ y''(0) \end{bmatrix} = \begin{bmatrix} 1 & 1 - e^{\frac{Voc}{a_1}} & 1 - e^{\frac{Voc}{a_2}} \\ 0 & e^{\frac{Voc}{a_1}}/a_1 & e^{\frac{Voc}{a_2}}/a_2 \\ 0 & -e^{\frac{Voc}{a_1}}/a_1^2 & -e^{\frac{Voc}{a_2}}/a_2^2 \end{bmatrix} \begin{bmatrix} I_L \\ I_{o_1} \\ I_{o_2} \end{bmatrix}.$$

Thus,

$$\begin{bmatrix} I_L \\ I_{o_1} \\ I_{o_2} \end{bmatrix} = \begin{bmatrix} 1 & 1 - e^{\frac{Voc}{a_1}} & 1 - e^{\frac{Voc}{a_2}} \\ 0 & e^{\frac{Voc}{a_1}}/a_1 & e^{\frac{Voc}{a_2}}/a_2 \\ 0 & -e^{\frac{Voc}{a_1}}/a_1^2 & -e^{\frac{Voc}{a_2}}/a_2^2 \end{bmatrix}^{-1} \begin{bmatrix} y(0) + V_{oc}/R_{sh} \\ y'(0) - 1/R_{sh} \\ y''(0) \end{bmatrix}.$$

In this way, with the same I-V characteristics data as shown in Figure5, we got $\theta_1 = 0.6849$, $\theta_2 = 2.2356$, $\theta_3 = 0.0247$, $\theta_4 = 3.3348$, $\theta_5 = 4.9034$ and $\theta_6 = 0.0010$. The two-diode model parameters are identified as

$$\begin{aligned} a_1 &= 1.8691 \text{ (V)}, \\ a_2 &= 0.3664 \text{ (V)}, \\ I_{o_1} &= 1.5168 \times 10^{-10} \text{ (A)}, \\ I_{o_2} &= 7.9060 \times 10^{-54} \text{ (A)}, \\ I_L &= 4.9480 \text{ (A)}, \\ R_{sh} &= 955.1229 \text{ } (\Omega), \\ R_s &= 0.6845 \text{ } (\Omega). \end{aligned}$$

The average absolute error $\bar{E} = 0.0080$ and $RMSE = 1.35\%$, both of which are slightly reduced as compared to the one-diode model result. As expected, I_{o_2} is indeed extremely close to zero, whereas other parameters are comparable to their counter parts in one-diode model result.

It should be highlighted that the diode model parameters derived from the indoor flash test are not constant. Actually, they are varying with temperature and solar radiation. Therefore, it is necessary to check the online computability of the proposed method for PV modules under non-constant environment, which is demonstrated by the outdoor module testing as follows.

4.2. Outdoor Module Testing

Outdoor module testing (OMT) is usually carried out by many PV panel manufacturers and solar research institutes for the module performance evaluation under the real operating environments. DC parameters including full I-V curves, V_{oc}, I_{sc}, V_{mpp}, I_{mpp}, P_{mpp} together with module temperature are measured and logged every minute. Environmental parameters including in-plane solar irradiance G_{si}, ambient temperature T_{amb}, module temperature T_{mod}, wind speed and wind direction are logged simultaneously with the DC parameters. Between I-V measurements, electrical energy is maintained at the module maximum power point (MPP). The uncertainty of all electrical measured parameters is within $\pm 0.1\%$ for full scale. With these I-V data in time series, the diode model parameters can be identified online by the proposed method and correlated to the environmental factors like irradiance, temperature, etc.

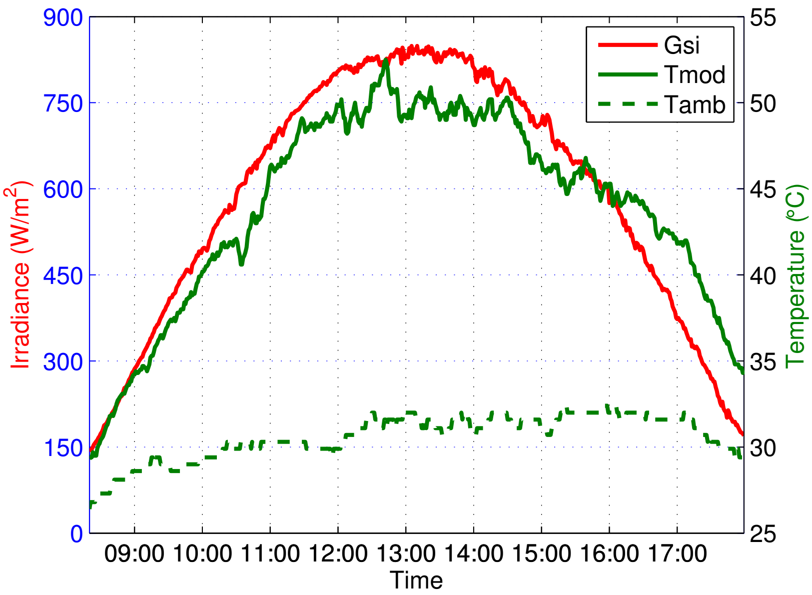

Figure 7. Environmental factors of a typical day in SERIS' OMT testbed.

Figure 7 shows the time series of G_{si}, T_{amb} and T_{mod} on a typical day from the OMT testbed of Solar Energy Research Institute of Singapore (SERIS). The plot is centred around the solar noon, which was at $13:10$ on the 5 August 2010.

By applying the proposed method in Section 3, the time-varying one-diode model parameters I_L, I_o, a, R_s and R_{sh} for the same day are identified, as shown in Figure 8. The variation of the identified parameters reflects the dynamics of the PV module under different environmental conditions, which cannot be seen from the static I-V curves.

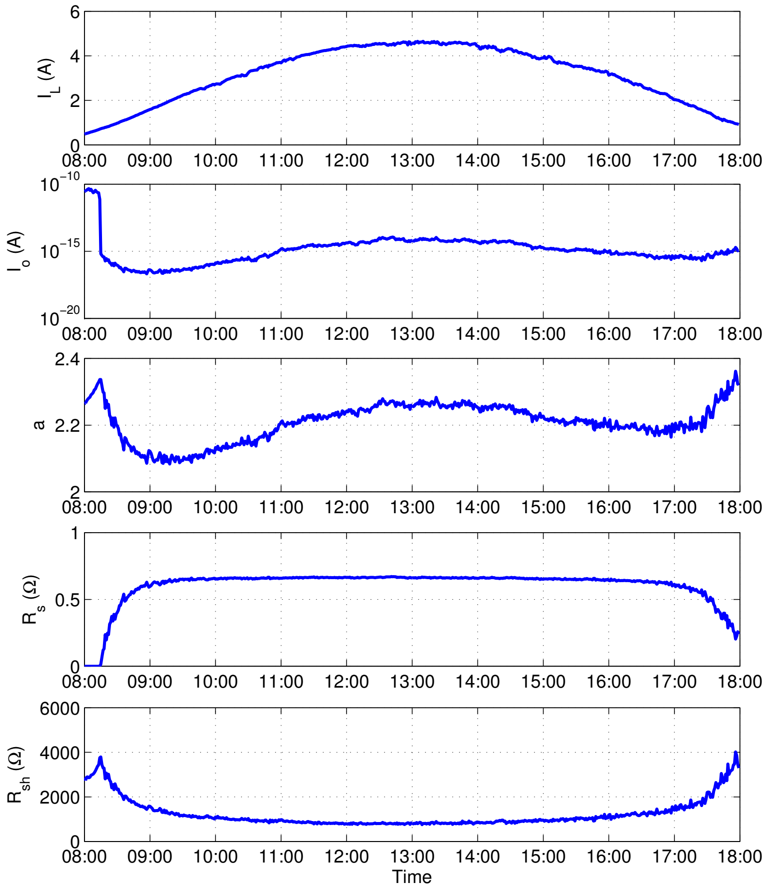

Figure 8. Identified one-diode model parameters.

The relationships between the identified parameters and the environmental operating conditions are further illustrated in Figure 9-12. A proportional relationship between I_L and irradiance intensity is observed in Figure 9. It is also apparent from Figure 10 that I_o generally shows an increasing trend with rising module temperature. This also agrees with the theoretical temperature dependence of I_o, as given by $I_o = BT^3 \mathrm{e}^{-E_g/(kT)}$, where E_g is the band gap of silicon and B is a temperature independent constant [14]. Figure 11 illustrates that a generally decreases with increasing irradiance for $G_{si} < 300$ W/m^2 and increases beyond that, which is as reported in [64]. When irradiance decreases in Figure 12, the series resistance R_s decreases and the shunt resistance R_{sh} increases, which is consistent with previous reported results [65]. The decrease in R_s is due to the decreased thermal loss ($I^2 R_s$) with decreasing irradiance.

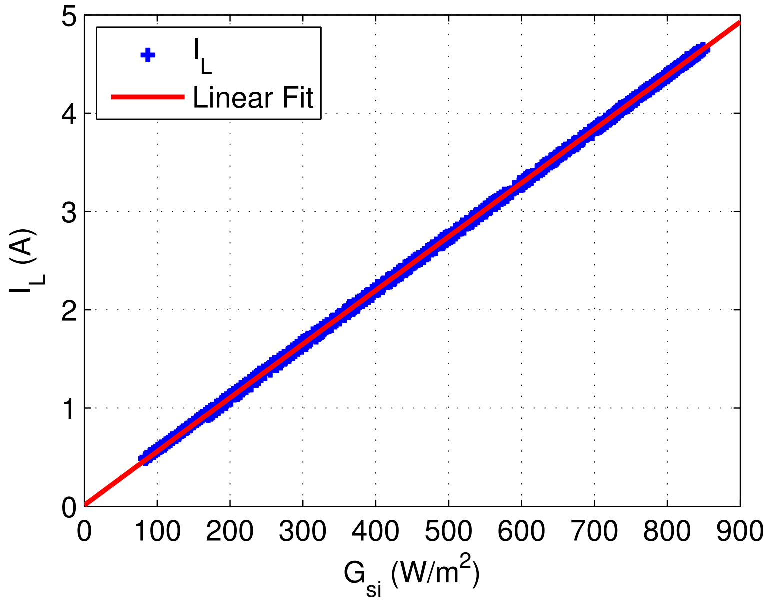

Figure 9. Proportional relationship between I_L and G_{si}.

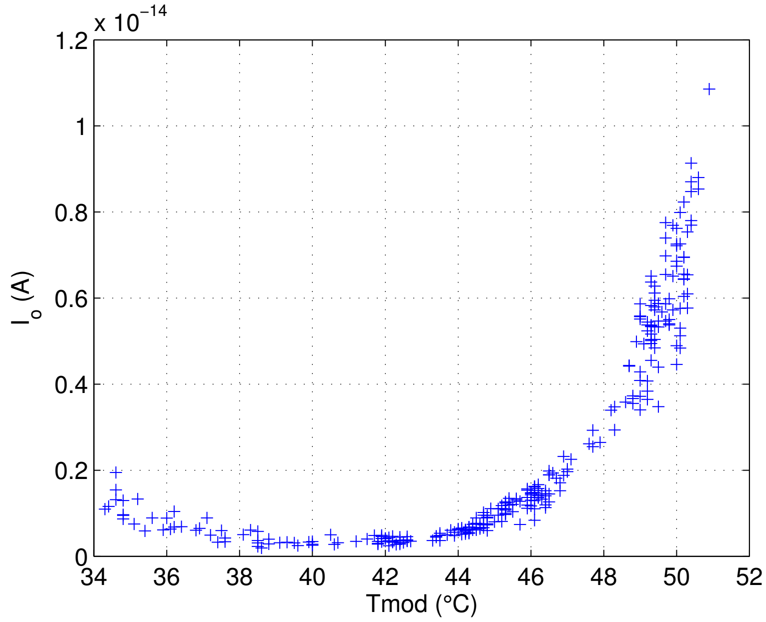

Figure 10. Relationship between I_o and T_{mod}.

The RMSE of the proposed algorithm in OMT case is shown in Figure13, where the burden of the online calculation for convergence (iterative steps for R_s until Tol or maxi-

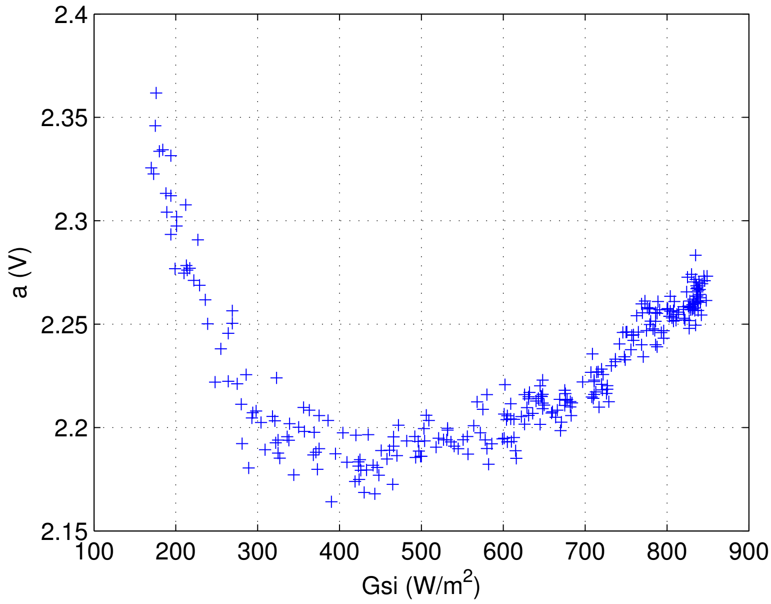

Figure 11. Relationship between a and G_{si}.

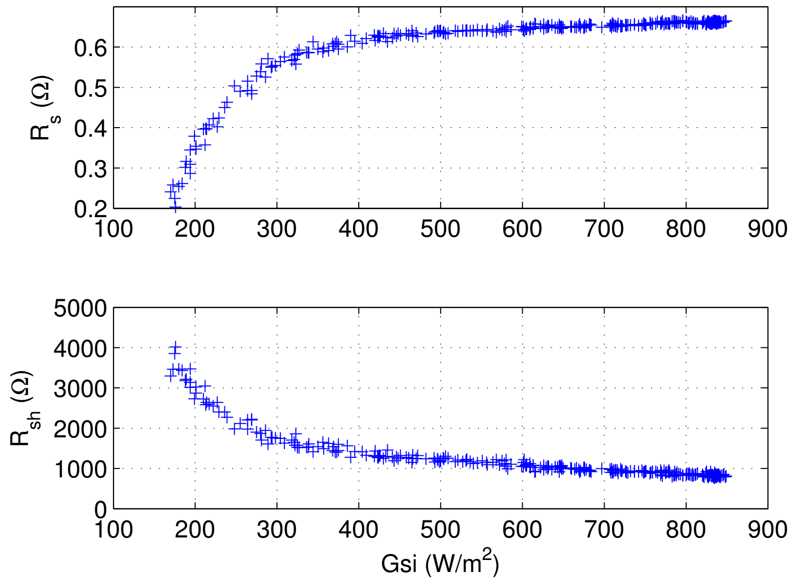

Figure 12. Relationship between R_s, R_sh and G_{si}.

mum cycle is achieved) is presented as well. Among 600 plus I-V scans during the day, there are only three cases with the RMSE exceeding the preset 1% Tol when the maximum number (100) of steps is reached. Even for these three cases, the RMSE is still below 1.5%. The iterative steps are very stable, and they are usually less than 30. This indicates that the online calculation burden of the proposed algorithm is low and the identification can be done by an industrial PC locally between two consecutive I-V scan (1 min in our case).

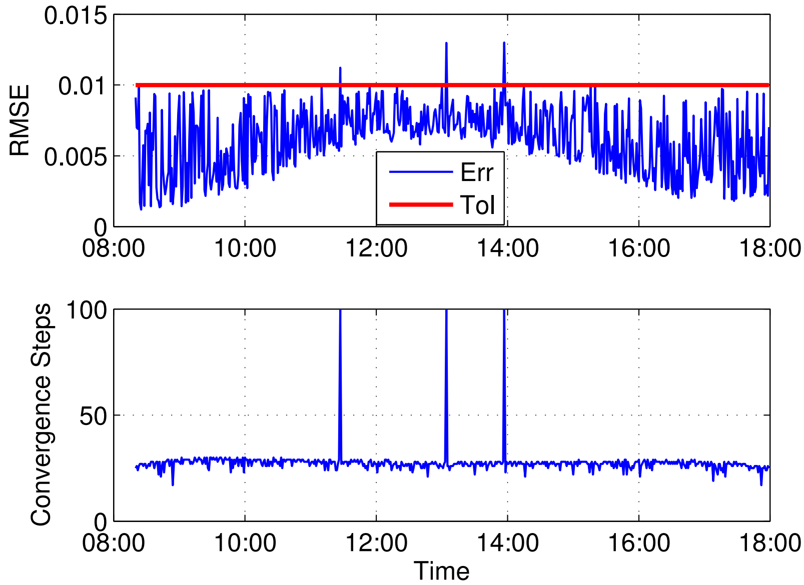

Figure 13. RMSE and burden of online calculation.

5. Comparison with Other Methods

In this section, the comparison of the proposed method with the approaches of iterative searching (based on Lambert W function) and evolutionary algorithms (mainly DE and GA) are discussed because they represent the most accurate estimation of PV model parameters.

5.1. Lambert W Function Based Method

In [32], two data sets of I-V curves (26 points) are presented, which are initially proposed in [39] and are commonly used to test the effectiveness of the extraction algorithms. One refers to a solar module (Photowatt-PWP 201) at $45°$C and the other refers to a solar cell (c-Si) at $33°$C, as shown in Table 1. The one-diode model parameters I_L, I_o and R_{sh} are proved to be functions of R_s and a. So the searching in the two-dimensional parameter space of R_s and a with the constrained conditions of (4), (5) and (7) yields Solution A; with the constrained conditions of (4), (5) and (6) yields Solution B. These two solutions are then fine tuned as the initial values of some nonlinear least square for the experimental data, which yields Solution C and D, respectively.

The comparison of the solutions of one-diode model by the propose and Lambert W function based method are shown in Table 2, where “MAE” is the mean absolute error and “Step” is the number of iterative searching cycle before convergence. It is clear to see that the proposed method gives a very close results to Lambert W function based method. Although the error is slightly bigger, the number of iteration steps is less.

Table 1. Experimental I-V data [32]

SN	Module		Cell	
	Voltage (V)	Current (A)	Voltage (V)	Current (A)
1	−1.9426	1.0345	−0.2057	0.7640
2	0.1248	1.0315	−0.1291	0.7620
3	1.8093	1.0300	−0.0588	0.7605
4	3.3511	1.0260	0.0057	0.7605
5	4.7622	1.0220	0.0646	0.7600
6	6.0538	1.0180	0.1185	0.7590
7	7.2364	1.0155	0.1678	0.7570
8	8.3189	1.0140	0.2132	0.7570
9	9.3097	1.0100	0.2545	0.7555
10	10.2163	1.0035	0.2924	0.7540
11	11.0449	0.9880	0.3269	0.7505
12	11.8018	0.9630	0.3585	0.7465
13	12.4929	0.9255	0.3873	0.7385
14	12.6490	0.9120	0.4137	0.7280
15	13.1231	0.8725	0.4373	0.7065
16	14.2221	0.7265	0.4590	0.6755
17	14.6995	0.6345	0.4784	0.6320
18	15.1346	0.5345	0.4960	0.5730
19	15.5311	0.4275	0.5119	0.4990
20	15.8929	0.3185	0.5265	0.4130
21	16.2229	0.2085	0.5398	0.3165
22	16.5241	0.1010	0.5521	0.2120
23	16.7987	−0.0080	0.5633	0.1035
24	17.0499	−0.1110	0.5736	−0.0100
25	17.2793	−0.2090	0.5833	−0.1230
26	17.4885	−0.3030	0.5900	−0.2100

Table 2. Solution comparison for solar module

Parameters	Proposed	Laudani 1A	Laudani 1B	Laudani 1C	Laudani 1D
I_L (A)	1.0334262	1.032173	1.033537	1.0323759	1.0323759
I_o (μA)	2.4424001	3.035367	2.825571	2.5188885	2.5188848
R_s (Ω)	1.2307473	1.218407	1.224053	1.2390187	1.2390187
R_{sh} (kΩ)	0.6034037	0.783516	0.689321	0.7456443	0.7456431
a ($N_s nkT_c/q$)	1.2975122	1.319345	1.312115	1.3002458	1.3002456
RMSE (10^{-3})	2.4777	2.1176	2.1547	2.0465	2.0465
MAE (10^{-3})	1.8461	1.6425	1.6060	1.6917	1.6917
Steps	8	12	10	19	28

The error mainly arises from the numerical integrations presented in Section 3.4 and the few I-V data samples available (26 points only). If more data samples on the I-V curve are known, the error of the proposed method will be reduced. To illustrate this point, model parameters from the solution of Laudani 1D was used to reproduce the whole I-V curve with the help of (16). The number of samples are selected to be 50, 100, 200. Based on such samples on the I-V curve derived from Laudani 1D solution, the RMSE of the proposed method to the whole I-V and the experimental data are shown in Table 3. As expected, the more data samples, the smaller RMSE. When data samples increased to 100, the RMSE for the experimental data is already better than the solutions of Laudani 1A/B and all the other results compared in [32].

Table 3. RMSE with different data samples (Module)

Source	Solutions	RMSE[1]	RMSE[2]	Steps
Module[3]	From 50 pts	3.3085×10^{-4}	2.2290×10^{-3}	8
	From 100 pts	8.5583×10^{-5}	2.0939×10^{-3}	13
	From 200 pts	2.0177×10^{-5}	2.0874×10^{-3}	12
Cell[4]	From 50 pts	3.6098×10^{-4}	9.9881×10^{-4}	8
	From 100 pts	8.8401×10^{-5}	8.6810×10^{-4}	9
	From 200 pts	2.2234×10^{-5}	8.5153×10^{-4}	10

[1] for the whole I-V curve [2] for the experimental data in [32]
[3] I-V curve is produced from Laudani 1D
[4] I-V curve is produced from Laudani 2D

The result comparison for the solar cell I-V data in [32] is shown in Table 4. The RMSE of the proposed method is smaller than the results of Laudani 2A/C, and only slightly bigger than Laudani 2B/D. When data samples increased to 100, the proposed method already outperformed Laudani 2B, as shown in Table 3.

Table 4. Solution comparison for solar cell

Parameters	Proposed	Laudani 2A	Laudani 2B	Laudani 2C	Laudani 2D
I_L (A)	0.7609438	0.764114	0.761060	0.7706871	0.7607884
I_o (μA)	0.3456572	0.003496	0.290125	0.003668522	0.3102482
R_s (mΩ)	36.14233	45.438	36.8	49.11298	36.55304
R_{sh} (Ω)	49.482205	11.103851	49.973561	11.103904	52.859056
a (10^{-2})	3.9256187	2.9929942	3.8784080	2.997888	3.8965248
RMSE (10^{-3})	1.0548	11.388	0.88437	8.9605	0.77301
MAE (10^{-3})	0.85202	9.4014	0.69732	7.2064	0.67810
Steps	8	8	7	14	16

In general, Lambert W function based method has many benefits in two aspects:

- It utilizes the Lambert W function to convert a non-concave optimal problem into a concave optimal problem;
- It utilizes reduced forms to decrease the dimension of the parameter space from five to two.

This method can deal with the I-V data from the data sheet (points at SC, OC, MPP) or experiment (full I-V curve), and in most of cases, it yields the best results in terms of RMSE and/or MAE.

The deficiencies of Lambert W function based method may be:

- No unique solutions;
- Inapplicable to the multi-diode model ($m > 1$) parameter identification due to the limitations of Lambert W function;
- Not easy to be implemented and unsuitable for online parameter identification.

The proposed method further reduces the dimension of the parameter space to one. It uses linear square other than nonlinear optimal algorithms to derive diode model parameters, so the drawbacks of nonlinear algorithms are avoided. It can also be used for multiple-diode model and simple enough to be implemented as online calculation. The deficiencies is that it requires the knowledge of the full I-V curve data.

5.2. Evolution Algorithms

As mentioned in the Introduction, evolution algorithms are very suitable for the search of a global optimal solution. Recently, two types of evolution algorithms using differential evolution (DE) [50] and genetic algorithm (GA) [45] yield good results for diode model parameter identification. Since no full I-V curve data are provided in [45, 50], we do the comparison in an indirect way as follows. Firstly, use the identified parameters (I_L, I_o, a, R_s and R_{sh}) to reconstruct the I-V curve by (16); Secondly, use that I-V curve data to identify diode-model parameters with the proposed method. Since DE and GA are applied to derive a, R_s and R_{sh} only (I_L and I_o are derived by formulas in [2,58]), we only compare the results of a, R_s and R_{sh}. Table 5 shows the results of a, R_s and R_{sh} from the proposed method and DE/GA. It is clear to see that the differences in between are very minor.

Table 5. Solution comparison with evolution algorithms

Module	**Solutions**	a ($N_s nkT_c/q$)	R_s (Ω)	R_{sh} (Ω)
Shell SM55	Proposed	1.2666	0.3001	2.3165×10^3
(mono-cSi)	DE	1.2665	0.3	2.34×10^3
Shell S75	Proposed	1.2300	0.2000	1.7834×10^3
(multi-cSi)	DE	1.2295	0.2	1.79×10^3
Sanyo 215	Proposed	2.1778	0.7821	851.2464
(HIT)	GA	2.1780	0.782	852.177
Kyocera 200	Proposed	1.5340	0.3310	882.7933
(multi-cSi)	GA	1.5337	0.331	883.925

The result of the two-diode model for the aforementioned Kyocera module (Kyocera - KC200GT) was also reported in [45]. It is interesting to comparing this result with ours.

If looking carefully at the comparison shown in Table 6, the GA algorithm gives comparable I_{o_1} and I_{o_2} (both in 10^{-9} A). a_1 and a_2 are also near to each other. If ignoring the differences between them, the two-diode can be combined as one. This implies that GA algorithm actually gives a result of one-diode model but mathematically divides it into two diodes format with no physical meaning. That's a common issue for the global optimization algorithm like DE and GA, whereas the proposed method has no such problems.

Table 6. Comparison of two-diode models

Parameters	GA	Proposed
a_1 (V)	1.5420	1.4936
a_2 (V)	1.9095	0.4944
R_s (Ω)	0.29	0.4095
R_{sh} (Ω)	480.496	842.8287
I_{o_1} (A)	4.23×10^{-9}	1.6044×10^{-9}
I_{o_2} (A)	9.1478×10^{-9}	2.6559×10^{-29}
MAE	0.02	0.0058

6. Graphical Meaning

In the previous sections, we showed the effectiveness of the proposed method to accurately extract diode model parameters from the I-V characteristics. This section illustrates the underlying principle from the angle of control theory by an illustration of the graphical meanings of the proposed method.

As control theory is usually studied for stable systems, coordinate transformation in Section 3.6 is applied, i.e., $\tilde{V} = V_{oc} - V$ so that I-$\tilde{V}$ is corresponding to some stable linear system. After transformation, I-V curve in Figure 4 is changed to I-$\tilde{V}$ (blue line) in Figure 14. Draw a straight line (black) starting from $O(0, 0)$ with the slope of $1/R_s$, i.e., $Y = X/R_s$, with the same I, the coordinates of the points on the black and blue lines will be $Q(R_sI, I)$ and $P(\tilde{V}, I)$, respectively. Therefore, $\tilde{x} = \tilde{V} - R_sI$ actually represents the distance between P and Q (green arrow). If $Y' = X/R_s$ is constructed as the new Y-axis, then only in XOY' coordinate system, I-$\tilde{V}$ curve is equivalent to a response of some linear system. In normal XOY coordinate system, this is not the case unless each point on the I-$\tilde{V}$ curve is shifted a variable distance of R_sI to the Y-axis, which is shown by red dash line in Figure 14.

Note that for the response of a stable linear system with zero initial conditions, both x and y values are monotonically increasing, which means distance $|PQ|$ is monotonically increasing with I. If $1/R_s < \mathrm{d}I/\mathrm{d}\tilde{V}|_{\tilde{V}=0} = -\mathrm{d}I/\mathrm{d}V|_{V=V_{oc}}$, the black line will intersect with the blue one so that the monotonically increasing of $|PQ|$ is violated, see Figure 15. Therefor, $1/R_s \geq -\mathrm{d}I/\mathrm{d}V|_{V=V_{oc}}$, which yields the upper bound of R_s discussed in Section 3.5

Figure 16 shows the impact of Rs on the RMSE of the proposed method, where I-V characteristic data are from the same indoor flash test module discussed in Section 4.1, and

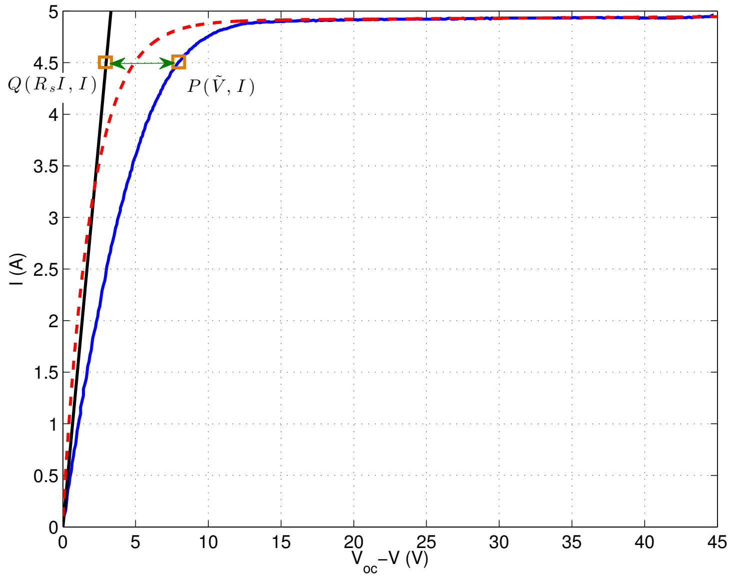

Figure 14. The I-$\tilde{V}$ characteristic from I-V.

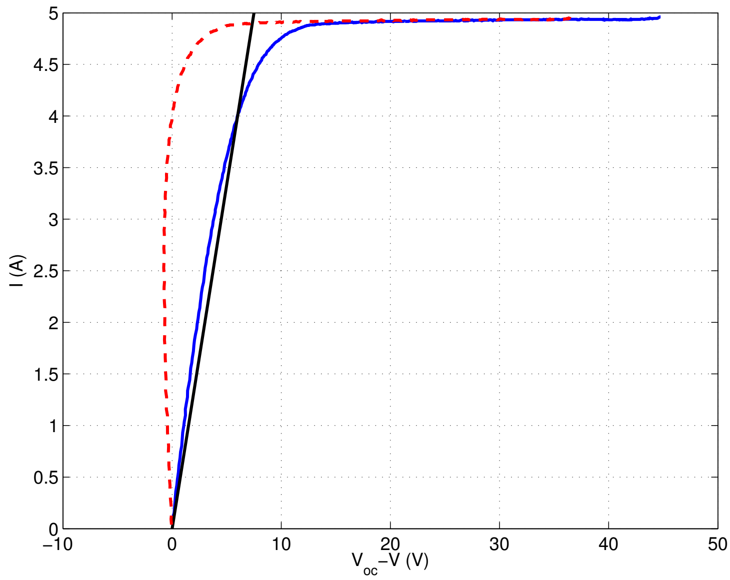

Figure 15. Impact of R_s on the profile of I-$\tilde{V}$.

$0 \leq R_s \leq -\mathrm{d}V/\mathrm{d}I|_{V=V_{oc}}$. One sees clearly that the accuracy of the proposed method is very sensitive to R_s, which implies that only when R_s is properly selected, the resulted I-$\tilde{V}$ is the response of a linear system. Such high sensitivity results in the unique solution of R_s and the rest of PV model parameters, and the effectiveness of the binary search algorithm proposed in Section 3.5.

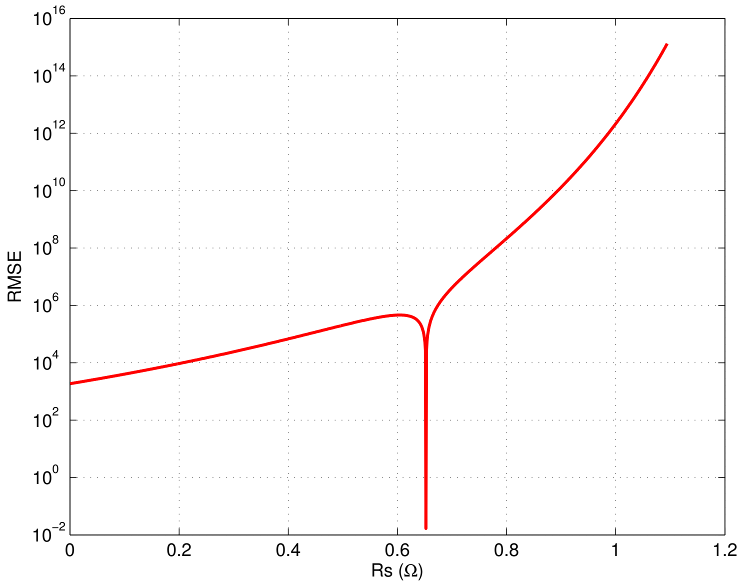

Figure 16. Impact of R_s on the RMSE of the proposed method.

7. Applications

7.1. Non-contact Measurement of POA Irradiance and Cell Temperature

Irradiance on plane of array (POA) and cell temperature are important to PV systems because system performance, evaluated by performance ratio (PR), is derived from them. Usually, silicon sensors are applied in PV systems to measure the irradiance level on POA, as shown in Figure 17. Their structure is composed of a high-quality mono-crystalline solar cell connected to a high accuracy shunt, which is the same as Figure 2, where I_L is the photocurrent proportional to the POA irradiance, the diode represents the mono-crystalline cell, and R_{sh} is the shunt. The low shunt ($R_{sh} = 0.1\Omega$) causes the cell to operate close to the short-circuit point, which makes $I_{sh} \to I_L$ so that POA irradiance can be calibrated from I_{sh} according to the proportionality.

Essentially, silicon sensors use an internal reference cell as a benchmark to sense the POA irradiance of PV modules/systems. The measurement accuracy highly depends on the differences between: 1) reference cell and PV modules; 2) I_L and I_{sh}. However, mismatch between reference cell and PV modules is inevitable and $I_L \neq I_{sh}$ although compensation measures for temperature are taken into account. All of them cause the mismatch error up to $\pm 5\%$, and the sensor needs to be recalibrated every two years to avoid the measurement shift caused by the degradation of reference cell.

A more accurate irradiance sensor is pyranometer, which covers the full spectrum of solar radiation (300-$2,800$ nm) from a field of view of 180 degrees. It is seldom deployed

Figure 17. POA irradiance measurement by silicon sensor.

in PV systems due to: 1) much higher cost as compared to silicon sensor; 2) mismatch in spectrum as crystalline is not a full spectrum absorber; 3) is not applicable to measure POA irradiance.

Temperature measurement for PV systems is even worse than POA irradiance measurement because what is measured is not the true cell temperature but the temperature of the back sheet of modules. This is because cells are encapsulated between the layers of glass, EVA, back sheet during the process of lamination. However, it is also impractical to incorporate a sensor within the module, in direct contact with an individual cell, to measure the cell temperature. In addition, the non-uniformity of module temperature across the module area, which was assumed to be $\pm 1\,^{\circ}\mathrm{C}$ in [66], is not accounted for with this approach. The current compromise is to put a sensor attached to the back sheet, which causes the cell temperature measurement to be roughly $2-3°$C lower than the true value. At a standard irradiance level of $1000W/m^2$, a mean cell-to-back temperature difference of $2.5 \pm 1\,^{\circ}\mathrm{C}$ was adopted in [67] for c-Si modules with plastic back encapsulation.

It is much desired to find a more accurate way to measure the POA irradiance and cell temperature as more and more PV systems are installed all over the world, not only for the academic research, but also for the commercial investment evaluation. Motivated by the recent progress in the diode model parameter identification [68, 69], photocurrent I_L and reverse saturation I_o can be linearly determined from the I-V characteristics of PV modules. Immediately, POA irradiance $G_s = \lambda I_L$, where λ is a constant slope (to be calibrated) and independent of irradiance or temperature [2]. Cell temperature T_c is derived from $I_o = BT_c^3 \mathrm{e}^{-E_g/(kT_c)}$, where E_g is the band gap of silicon and B is a temperature independent constant [14]. No external sensors for irradiance or temperature is required once the I-V curve is known.

7.1.1. Calibration of POA Irradiance

As mentioned before, the photocurrent I_L is proportional to POA irradiance G_s, i.e., $G_s = \lambda I_L$, and λ is the slope. To calibrate λ, the I-V characteristics of a full-sized commercial module were measured indoor by a PASAN IIIB with the constant illumination intensity of $200, 400, 600, 800, 1000, 1200 W/m^2$. The temperature for such flash tests is fixed at $25°$C.

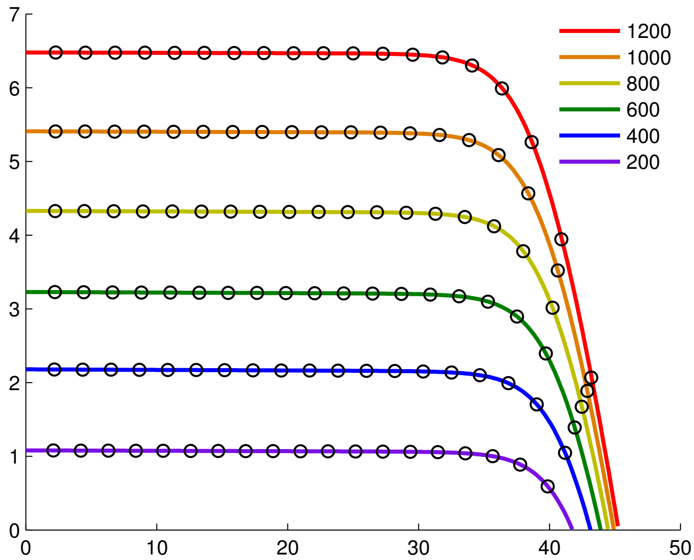

Figure 18. Indoor flash test at different illumination intensity.

Table 7. Identification results

Illumination (**W/m^2**)	I_L (A)	I_o (10^{-9}A)	a (V)	R_s (Ω)	R_{sh} (kΩ)	**RMSE** ($\times 10^{-3}$)
200	1.08	0.4782	1.9411	0.5293	1.8321	0.0849
400	2.18	0.4757	1.9407	0.6278	1.3512	0.1410
600	3.23	0.4745	1.9404	0.6339	1.3414	0.1809
800	4.33	0.4741	1.9401	0.6345	1.5710	0.2130
1000	5.41	0.4725	1.9399	0.6347	1.8408	0.2380
1200	6.48	0.4786	1.9397	0.6347	2.1330	0.2569

Figure 18 shows the family I-V characteristic of a PV module (crystalline) from the proposed indoor flash test, where estimation results by the identification method from Section 3 are indicated by circles. The estimation results obtained from the identified diode model parameters match closely to the I-V curves from the indoor flash test. The identified diode model parameters and RMSE compared to the real I-V curves are listed in Table 7, which illustrate the accuracy of the proposed identification.

Based on the results from Table 7, Figure 19 shows the correlation between G_s and I_L. As expected, I_L is proportional to G_s. The non-zero intercept is caused by measurement error, which brings the uncertainty of irradiance estimation up to $0.006/0.0054 = 1.11$ W/m^2. The slope λ from $G_s = \lambda I_L$ is determined by $\lambda = 1/0.0054 = 185.1852$.

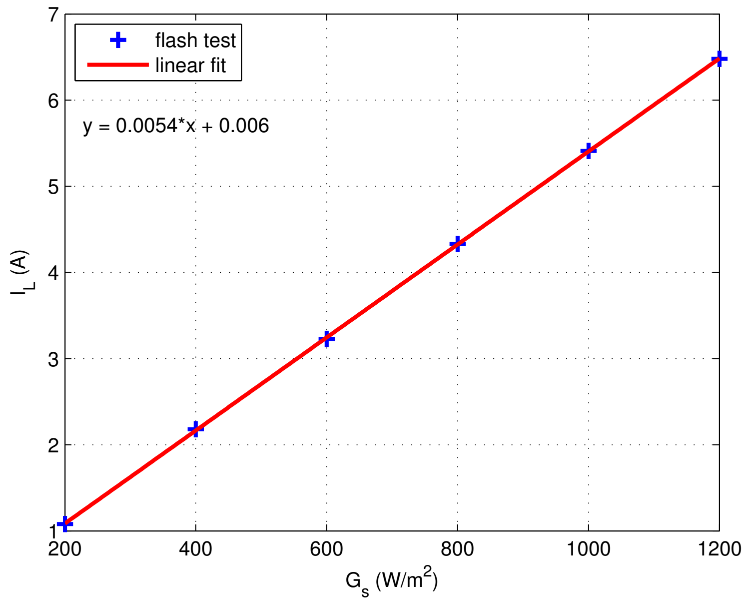

Figure 19. Determination of λ from $G_s = \lambda I_L$.

7.1.2. Calibration of Cell Temperature

Cell temperature is derived from $I_o = BT_c^3 \mathrm{e}^{-E_g/(kT_c)}$, where E_g is the band gap of silicon and B is a temperature independent constant [14]. Both B and E_g are required to be calibrated. To do the calibration, the I-V characteristics of the same module in Section 7.1.1 were measured by the PASAN IIIB in a thermal chamber. The illumination intensity is fixed at $1000W/m^2$ and the chamber temperature are set at $15°C$, $25°C$, $35°C$, $45°C$, $55°C$, $65°C$.

Figure 20 shows the results of the flash test at different temperature levels, where the circles represent the estimated I-V curves by the proposed identification. The identified diode model parameters and RMSE compared to the real I-V curves are listed in Table 8.

Table 8. Identification results

Temperature (°C)	I_L (A)	I_o (10^{-9}A)	a (V)	R_s (Ω)	R_{sh} (kΩ)	**RMSE** ($\times 10^{-3}$)
15	5.38	0.0326	1.7970	0.6326	1.8486	0.2676
25	5.41	0.4756	1.9399	0.6347	1.8409	0.2375
35	5.43	5.8101	2.0883	0.6367	1.8335	0.2089
45	5.45	61.544	2.2420	0.6378	1.8283	0.1810
55	5.48	564.16	2.4012	0.6388	1.8180	0.1550
65	5.50	4546.3	2.5659	0.6399	1.8075	0.1305

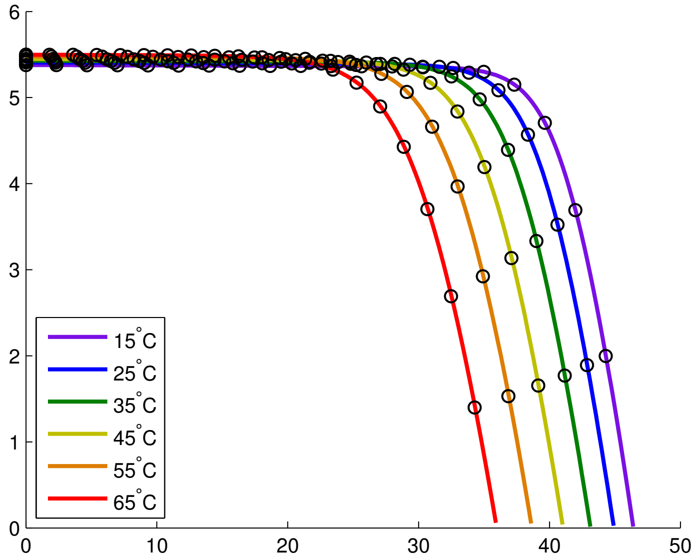

Figure 20. Indoor flash test at different temperatures.

With the identified I_o from Table 8, taking logarithmic to I_o gives,

$$\ln I_o = \ln B + 3\ln T_c - \frac{E_g}{kT_c}, \quad \Rightarrow$$

$$\ln I_o - 3\ln T_c = -\frac{E_g}{k}T_c^{-1} + \ln B. \tag{56}$$

Let $y = \ln I_o - 3\ln T_c$, $x = 1/T_c$, $\alpha = -E_g/k$ and $\beta = \ln B$, (56) becomes $y = \alpha x + \beta$. The relationship between x and y are shown in Figure 21. With linear fitting, $\alpha = -22122$ and $\beta = 35.637$. Thus, $E_g = -k\alpha = 3.0543 \times 10^{-19}$ and $B = \mathrm{e}^{\beta} = 2.9988 \times 10^{15}$. After E_g and B are known, the cell temperature T_c can be numerically determined by Newton-Raphson method with the initial $T_c = 300$ K.

7.1.3. Outdoor Verification

To validate the proposed non-contact measurement for POA irradiance and cell temperature, the same module after the indoor calibration was put at outdoor module testing bed for a whole day with the continuous recording of I-V curves and meteorological data. By applying the proposed method in Section 3, the time-varying one-diode model parameters I_L, I_o, a, R_s and R_{sh} for the same day are identified, which has been discussed in Section 4.2 and the results are shown in Figure 8. The variation of the identified parameters reflects the dynamics of the PV module under different environmental conditions, which cannot be seen from the static I-V curves. With the identified diode model parameters, the POA irradiance and cell temperature can then be derived.

Based on the calibration value λ from Section 7.1.1, the POA irradiance can be determined from I_L by $G_s = \lambda I_L$. Figure 22 illustrates the comparison to the results from a

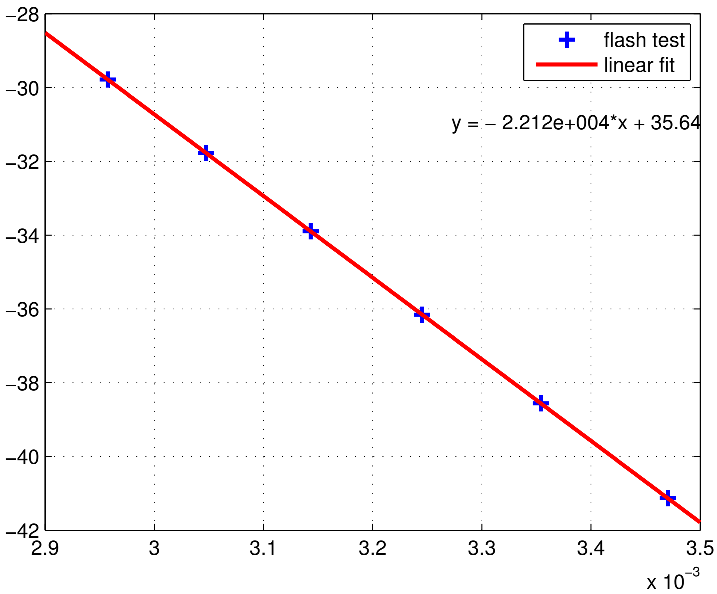

Figure 21. Calibration of E_g and B.

reference silicon sensor which has the same inclined angle as the PV module. As seen from Figure 22, the non-contact measurement POA irradiance matches the irradiance measurement from the silicon sensor well.

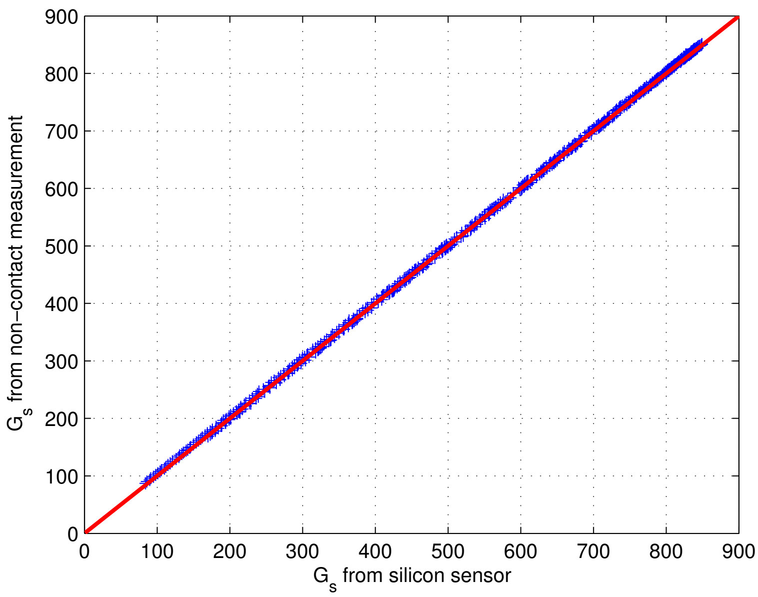

Figure 22. POA irradiance: non-contact measurement vs. reference cell.

With the calibrated E_g and B from Section 7.1.2, cell temperature T_c is numerically determined by Newton-Raphson method. The comparison between T_c and T_{mod} (backsheet measurement) is shown in Figure 23. One can see that when irradiance increases in the morning, T_c is usually higher than T_{mod}, which is due to the positive temperature gradient (from cell to backsheet) during that time. Whereas after solar noon when irradiance decreases, temperature gradient becomes negative due to the thermal delay, so T_c is lower than T_{mod}. But the difference in between is within $\pm 2°$C.

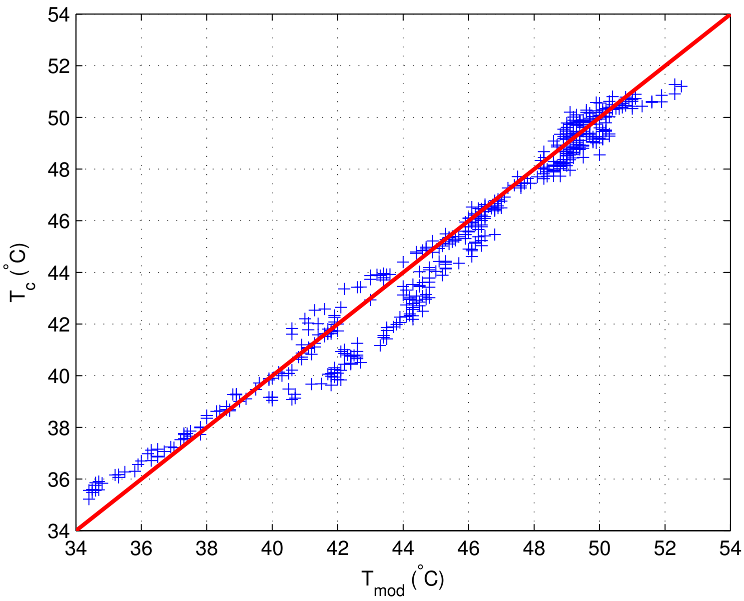

Figure 23. Cell temperature: non-contact measurement vs. backsheet-attached sensors.

7.2. PV Panel Characterisation for Satellites

When PV panels are used in satellites, it is usually not allowed to do the flash test sweeping from OC to SC because the power supply must be stable to maintain the normal operation of satellites. Hence, to do the PV panel characterisation for satellites in operation, I-V scan is limited within a small range around MPP, i.e., $I \in [I_1, I_2]$ and $V \in [V_1, V_2]$. With the example of one-diode model, it follows from (3) that

$$I_1 = I_L + I_o - I_o \mathrm{e}^{\frac{V_1 + R s I_1}{a}} - \frac{V_1 + R_s I_1}{R_{sh}}, \tag{57}$$

$$I = I_L + I_o - I_o \mathrm{e}^{\frac{V + R s I}{a}} - \frac{V + R_s I}{R_{sh}}. \tag{58}$$

Let $\Delta I = I - I_1$ and $\Delta V = V - V_1$, (58) – (57) yields

$$\Delta I = I_o \mathrm{e}^{\frac{V_1 + R s I_1}{a}} \left(1 - \mathrm{e}^{\frac{\Delta V + R s \Delta I}{a}}\right) - \frac{\Delta V + R_s \Delta I}{R_{sh}}. \tag{59}$$

Let $y = \Delta I$ and $x = \Delta V + R_s \Delta I$, (59) becomes

$$y = I_o \mathrm{e}^{\frac{V_1 + RsI_1}{a}} \left(1 - \mathrm{e}^{\frac{x}{a}}\right) - \frac{x}{R_{sh}}. \tag{60}$$

Taking differential once for (60) gives

$$\frac{\mathrm{d}y}{\mathrm{d}x} = -\frac{I_o}{a} \mathrm{e}^{\frac{V_1 + RsI_1}{a}} \mathrm{e}^{\frac{x}{a}} - \frac{1}{R_{sh}}. \tag{61}$$

Differentiating twice gives

$$\frac{\mathrm{d}^2 y}{\mathrm{d}x^2} = -\frac{I_o}{a^2} \mathrm{e}^{\frac{V_1 + RsI_1}{a}} \mathrm{e}^{\frac{x}{a}}. \tag{62}$$

Eliminating $\mathrm{e}^{x/a}$ from (61) and (62) gives

$$a\frac{\mathrm{d}^2 y}{\mathrm{d}x^2} - \frac{\mathrm{d}y}{\mathrm{d}x} = \frac{1}{R_{sh}},$$

which is just the same as (21). The remaining procedures are very similar to what we did in Section 2.1 except for the initial conditions. From (60) and (61), $y(0) = 0$ and $y'(0) = -I_o \mathrm{e}^{(V_1 + R_s I_1)/a}/a - 1/R_{sh}$, respectively. According to (24), the transfer function

$$G(s) = \frac{ay(0)s^2 + [ay'(0) - y(0)]s + \frac{1}{R_{sh}}}{as^2 - s} = \frac{-(I_o \mathrm{e}^{\frac{V_1 + RsI_1}{a}} + \frac{a}{R_{sh}})s + \frac{1}{R_{sh}}}{as^2 - s}.$$

The corresponding time domain differential equation is

$$a\frac{\mathrm{d}^2 y(t)}{\mathrm{d}t^2} - \frac{\mathrm{d}y(t)}{\mathrm{d}t} = -\left(I_o \mathrm{e}^{\frac{V_1 + RsI_1}{a}} + \frac{a}{R_{sh}}\right)\frac{\mathrm{d}u(t)}{\mathrm{d}t} + \frac{u(t)}{R_{sh}}, \tag{63}$$

where $t = x$ and $u(t) \equiv 1$. With the help of double integral in (39), (63) is equivalent to

$$ay(t) + \left(I_o \mathrm{e}^{\frac{V_1 + RsI_1}{a}} + \frac{a}{R_{sh}}\right) \int_{[0,t]}^{(1)} u(\tau) - \frac{1}{R_{sh}} \int_{[0,t]}^{(2)} u(\tau) = \int_{[0,t]}^{(1)} y(\tau).$$

Let $\theta = [a, I_o \mathrm{e}^{\frac{V_1 + RsI_1}{a}} + \frac{a}{R_{sh}}, \frac{1}{R_{sh}}]^T$, $\phi(t) = [y(t), \int_{[0,t]}^{(1)} u(\tau), -\int_{[0,t]}^{(2)} u(\tau)]^T$ and $\gamma(t) = \int_{[0,t]}^{(1)} y(\tau)$, then the least square solution for θ is given by

$$\theta = \left(\Phi^T \Phi\right)^{-1} \Phi^T \Gamma,$$

where $\Phi = [\phi(t_1), \cdots, \phi(t_N)]^T$ and $\Gamma = [\gamma(t_1), \cdots, \gamma(t_N)]^T$. Thus,

$$\begin{aligned} a &= \theta_1, \\ I_o &= (\theta_2 - \theta_1\theta_3)\mathrm{e}^{-\frac{V_1 + RsI_1}{\theta_1}}, \\ R_{sh} &= \frac{1}{\theta_3}. \end{aligned}$$

R_s is determined by the same binary search algorithm in Section 3.5 as before, and I_L is derived from (57) as follows once I_o, a, R_s and R_{sh} are all determined.

$$I_L = I_1 - I_o + I_o \mathrm{e}^{\frac{V_1 + RsI_1}{a}} + \frac{V_1 + R_s I_1}{R_{sh}}.$$

8. Conclusion

In this chapter, an approach on linear system identification is developed, which links the diode model parameters to the transfer function coefficients of a dynamic system. This approach solves the PV model parameters by an integral-based linear least square method, which reduces the dimension of the search space from 5 to 1, so the drawbacks of nonlinear algorithms are avoided. Graphical meanings of the proposed method are illustrated to help readers understand the underlying principles. Finally, a discussion of the possible applications of the proposed method like online PV monitoring and diagnostics, non-contact measurement of POA irradiance and cell temperature, fast model identification for satellite PV panels are presented.

References

[1] William Shockley. The theory of p-n junctions in semiconductors and p-n junction transistors. *The Bell System Technical Journal*, 28(3):435489, July 1949.

[2] W. De Soto, S.A. Klein, and W.A. Beckman. Improvement and validation of a model for photovoltaic array performance. *Sol. Energy*, 80(1):7888, 2006.

[3] J. Surya Kumari and Ch. Sai Babu. Mathematical modeling and simulation of photovoltaic cell using matlab-simulink environment. *International Journal of Electrical and Computer Engineering (IJECE)*, 2(1):2634, February 2012.

[4] Jing Jun Soon, Kay-Soon Low, and Shu Ting Goh. Multi-dimension diode photovoltaic (PV) model for different PV cell technologies. In *IEEE 23rd ISIE*, pages 24962501, 2014.

[5] B. G. Streetman and S. Banerjee. *Solid state electronic devices*. Prentice Hall, New Jersey, 5th edition, 2000.

[6] K. R. McIntosh. Lumps, humps and bumps: three detrimental effects in the current-voltage curve of silicon solar cells. PhD thesis, University of New SouthWales, 2001.

[7] D. Macdonald and A. Cuevas. Reduced fill factors in multicrystalline silicon solar cells due to injection-level dependent bulk recombination lifetime. *Prog. Photovolt: Res. Appl.*, (8):363375, 2000.

[8] F. Pelanchon, P. Mialhe, and J.P. Charles. The photocurrent and the open-circuit voltage of a silicon solar cell. *Sol. Cells*, 28(1):4155, 1990.

[9] N.M. Ravindra and Basudev Prasad. Saturation current in solar cells: an analysis. *Sol. Cells*, 2(2):109113, 1980.

[10] N. Santakrus Singh, Amit Jain, and Avinashi Kapoor. Determination of the solar cell junction ideality factor using special trans function theory (STFT). *Sol. Energ. Mat. Sol. C.*, 93(8):14231426, 2009.

[11] Chan DS and Phang JC. Analytical methods for the extraction of solar cell single- and double-diode model parameters from i-v characteristics. *IEEE Trans. Electron Devices*, 34(2):286293, 1987.

[12] D. Pysch, A. Mette, and S.W. Glunz. A review and comparison of different methods to determine the series resistance of solar cells. *Sol. Energ. Mat. Sol. C.*, 91(18):16981706, 2007.

[13] D. Sera and R. Teodorescu. Robust series resistance estimation for diagnostics of photovoltaic modules. In 35th IEEE IECON, pages 800805, 2009.

[14] Georgi Hristov Yordanov, Ole-Morten Midtgøard, and Tor Oskar Saetre. Series resistance determination and further characterization of c-si PV modules. *Renew. Energ.*, 46(10):7280, 2012.

[15] Yong Sin Kim, Sung-Mo Kang, Bruce Johnston, and RolandWinston. A novel method to extract the series resistances of individual cells in a photovoltaic module. *Sol. Energ. Mat. Sol. C.*, 115(8):2128, 2013.

[16] A. Chatterjee, A. Keyhani, and D. Kapoor. Identification of photovoltaic source models. *IEEE Trans. Energy Convers.*, 26(3):883889, Sep. 2011.

[17] Hadj Arab A, Chenlo F, and Benghanem M. Loss-of-load probability of photovoltaic water pumping systems. *Solar Energy*, 76:713723, 2004.

[18] Antonino Laudani, Francesco Riganti Fulginei, and Alessandro Salvini. Identification of the one-diode model for photovoltaic modules from datasheet values. *Sol. Energy*, 108:432446, 2014.

[19] de Blas MA, Torres JL, Prieto E, and Garía A. Selecting a suitable model for characterizing photovoltaic devices. *Renew. Energ.*, 25:371380, 2002.

[20] Lo Brano V, Orioli A, Ciulla G, and Di Gangi A. An improved five-parameter model for phtotvoltaic modules. *Sol. Energ. Mat. Sol. C.*, 94:13581370, 2010.

[21] Orioli A and Di Gangi A. A procedure to calculate the five-parameter model of crystalline silicon photovoltaic modules on the basis of the tabular performance data. *Appl. Energ.*, 102(1160-1177), 2013.

[22] S. Lineykin, Averbukh M, and A. Kuperman. An improved approach to extract the single-diode equivalent circuit parameters of a photovoltaic cell/panel. *Renew. Sustain. Energy. Rev.*, 30:282289, 2014.

[23] Peng L, Sun Y, and Meng Z. An improved model and parameters extraction for photovoltaic cells using only three state points at standard test condition. *J. Power Sources*, 248(621-631), 2014.

[24] S. Lineykin and A. Kuperman. Issues in modeling amorphous silicon photovoltaic modules by single-diode equivalent circuit. *IEEE Trans. Ind. Electron.*, 61(99), 2014.

[25] Y. A. Mahmoud, W. Xiao, and H. H. Zeineldin. A parameterization approach for enhancing PV model accuracy. *IEEE Trans. Ind. Electron.*, 60(12):57085716, 2013.

[26] F. Adamo, F. Attivissimo, A. Di Nisio, and M. Spadavecchia. Characterization and testing of a tool for photovoltaic panel modeling. *IEEE Trans. Instrum. Meas.*, 60(5):16131622, May 2011.

[27] Y. Mahmoud, W. Xiao, and H. H. Zeineldin. A simple approach to modeling and simulation of photovoltaic modules. *IEEE Trans. Sustain. Energy*, 3(1):185186, Jan. 2012.

[28] S. Lineykin, M. Averbukh, and A. Kuperman. Five-parameter model of photovoltaic cell based on STC data. In 27th IEEE Conv. Electr. Electron. Eng., pages 15, Eilat, Israel, Nov. 2012.

[29] A. Izadian, A. Pourtaherial, and S. Motahari. Basic model and governing equation of solar cells used in power and control applications. In IEEE Energy Conv. Congr. Expo., pages 14831488, Raleigh, NC, Sep. 2012.

[30] F. Ghani, M. Duke, and J. Carson. Numerical calculation of series and shunt resistances and diode quality fator of a photovoltaic cell using the Lambert W-function. *Sol. Energy*, 91:422431, 2013.

[31] F. Ghani, M. Duke, and J. Carson. Numerical calculation of series and shunt resistance of a photovoltaic cell using the Lambert W-function: Experimental evaluation. *Sol. Energy*, 87:246253, 2013.

[32] Antonino Laudani, Francesco Riganti Fulginei, and Alessandro Salvini. High performing extracton procedure for the one-diode model of a photovoltaic panel from experimental I-V curves by using reduced forms. *Sol. Energy*, 103:316326, 2014.

[33] M. Al-Rashidi, M. Al-Hajri, K. El-Naggar, and A. Al-Othman. A new estimation approach for determining the I-V characteristics of solar cells. *Sol. Energy*, 85(7):15431550, 2011.

[34] H. Qin and J. W. Kimball. Parameter determination of photovoltaic cells from field testing data using particle swarm optimization. In *IEEE PECI*, number 1-4, 2011.

[35] Jing Jun Soon and Kay-Soon Low. Optimizing photovoltaic model parameters for simulation. In *IEEE 21st ISIE*, pages 18131818, 2012.

[36] Y. Li, W. Huang, H. Huang, C. Hewitt, Y. Chen, G. Fang, and D. Carroll. Evaluation of methods to extract parameters from current-voltage characteristics of solar cells. *Sol. Energy*, 90:5157, Apr. 2013.

[37] Kien F. Teng and Ping Wu. PV module characterization using Q-R decomposition based on the least square method. *IEEE Trans. Ind. Electron.*, 36(1):7175, 1989.

[38] Hyeonah Park and Hyosung Kim. PV cell modeling on single-diode equivalent circuit. In *39th IEEE IECON*, pages 18451849, 2013.

[39] T. Easwarkhanthan, J. Bottin, I. Bouhouch, and C. Boutrit. Nonlinear minimization algorithm for determining the solar cell parameters with microcomputers. *Int. J. Solar Energ.*, 4:112, 1986.

[40] Dkhichi F, Oukarfi B, Fakkar A, and Belbounaguia N. Parameter identification of solar cell model using levenberg-marquardt algorithm combined with simulated annealing. *Sol. Energy*, 110:781788, 2014.

[41] Zhang K, Jia W, Koplowitz J, Marzocca P, and Cheng MC. Modeling of photovoltaic cells and arrays based on singular value decomposition. *Semicond. Sci. Technol.*, 28(3):035002, 2013.

[42] J. Appelbaum, A. Chait, and D. Thompson. Parameter estimation and screening of solar cells. *Prog. Photovolt: Res. Appl.*, 1(2):93106, February 1993.

[43] Jervase JA, Bourdoucen H, and Al-Lawati A. Solar cell parameter extraction using genetic algorithms. Meas. *Sci. Technol.*, 12(11):1922, 2001.

[44] Zagrouba M, Sellami A, Bouaïcha M, and Ksouri M. Identification of PV solar cells and modules parameters using the genetic algorithms: application to maximum power extraction. *Sol. Energy*, 84(5):860866, 2010.

[45] M. S. Ismail, M. Moghavvemi, and T. M. I. Mahlia. Characterization of pv panel and global optimization of its model parameters using genetic algorithm. *Energ. Convers. Manage.*, 73:1025, 2013.

[46] Dizqah A.M., Maheri A., and Busawon K. An accurate method for the PV model identification based on a genetic algorithm and the interior-point method. *Renew. Energ.*, 72:212222, 2014.

[47] Wang X.M. and Xu Y. Parameter extraction of solar cells using particle swarm optimization. *J. Appl. Phys.*, 105(9):094502, 2009.

[48] Jing Jun Soon and Kay-Soon Low. Photovoltaic model identification using particle swarm optimization with inverse barrier constraint. *IEEE Trans. Power Electron.*, 27(9):39753983, Sep. 2012.

[49] Khanna V, Das BK, Bisht D, and Singh PK. A three diode model for industrial solar cells and estimation of solar cell parameters using pso algorithm. *Renew. Energ.*, 78:105113, 2015.

[50] K Ishaque and Z. Salam. An improved modeling method to determine the model parameters of photovoltaic (PV) modules using differential evolution (DE). *Sol. Energy*, 85:23492359, 2011.

[51] W. Gong and Z. Cai. Parameter extraction of solar cell models using repaired adaptive differential evolution. *Sol. Energy*, 94:209220, 2013.

[52] L.L Jiang, D.L. Maskell, and J.C. Patra. Parameter estimation of solar cells and modules using an improved adaptive differential evolution algorithm. *Appl. Energ.*, 112:185193, 2013.

[53] Asif S. and Li Y. Solar cell modeling and parameter optimization using simulated annealing. *J. Propuls Power*, 24(5):10181022, 2008.

[54] K. El-Naggar, M. AlRashidi, M. AlHajri, and A. Al-Othman. Simulated annealing algorithm for photovoltaic parameters identification. *Sol. Energy*, 86:266274, 2012.

[55] Celik AN. Artificial neural network modeling and experimental verification of the operating current of mono-ctystalline photovoltaic modules. *Sol. Energy*, 85(10):25072517, 2011.

[56] Almonacid F, Rus C, Hontoria L, Fuentes M, and Nofuentes G. Characterisation if Sicrystalline PV modules by artificial neural networks. *Renew. Energ.*, 34(4):941949, 2009.

[57] W. Xiao, P. R. Dunford, W. G. Palmer, and A. Capel. Regulation of photovoltaic voltage. *IEEE Trans. Ind. Electron.*, 54(3):13651374, 2007.

[58] M. G. Villalva, J. R. Gazoli, and Filho E. R. Comprehensive approach to modeling and simulation of photovoltaic arrays. *IEEE Trans. Power Electron.*, 24(5):11981208, 2009.

[59] Soon J.J. and Low K.S. Optimizing photovoltaic model for different cell technologies using a generalized multi-dimension diode model. *IEEE Trans. Ind. Electron.*, 62(10):63716380, 2015.

[60] Debashisha Jena and Vanjari Venkata Ramana. Modeling of photovoltaic system for uniform and non-uniform irradiance: A critial review. *Renew. Sustain. Energy. Rev.*, 52:400417, 2015.

[61] Vun Jack Chin, Zainal Salam, and Kashif Ishaque. Cell modeling and model parameters estimation techniques for phtotvoltaic simulation application: A review. *Appl. Energ.*, 154:500519, 2015.

[62] K. Ogata. *Modern Control Engineering*. Prentice Hall, 2002.

[63] Qing-Guo Wang and Yong Zhang. Robust identification of continuous systems with dead-time from step responses. *Automatica*, 37(3):377390, 2001.

[64] M. Hamdy and R. Call. The effect of the diode ideality factor on the experimental determination of series resistance of solar cells. *Sol. Cells*, 20(2):119126, 1987.

[65] M. C. Di Piazza and G. Vitale. *Photovoltaic Sources: Modeling and Emulation*. Springer, 2012.

[66] W. Zaaiman H. Mullejans and R. Galleano. Analysis and mitigation of measurement uncertainties in the traceability chain for the calibration of photovoltaic devices. *Measurement Science and Technology*, 20, 2009.

[67] K. Whitfield and C.R. Osterwald. Procedure for determining the uncertainty of photovoltaic module outdoor electrical performance. *Progress in Photovoltaics: Research & Applications*, 9:87 102, 2001.

[68] Li Hong Idris Lim, Zhen Ye, Jiaying Ye, Dazhi Yang, and Hui Du. A linear identification of diode models from single I-V characteristics of PV panels. *IEEE Trans. Ind. Electron.*, 62(7):41814193, 2015.

[69] Li Hong Idris Lim, Zhen Ye, Jiaying Ye, Dazhi Yang, and Hui Du. A linear method to extract diode model parameters of solar panels from a single I-V curve. *Renewable Energy*, 76:135142, 2015.